

The X-ray absorption spectrum of the propargyl radical, $C_3H_3 \cdot$

Dorothee Schaffner,¹ Theo Juncker von Buchwald,² Jacob Pedersen,^{2,3} Andreas Rasp,¹ Emil Karaev,¹ Valentin von Laffert,¹ Alessio Bruno,⁴ Michele Alagia,⁵ Stefano Stranges,^{5,4} Ingo Fischer,^{1, a)} and Sonia Coriani^{2, b)}

¹⁾ *Institute of Physical and Theoretical Chemistry, University of Würzburg, D-97074 Würzburg, Germany.*

²⁾ *DTU Chemistry, Technical University of Denmark, DK-2800 Kgs. Lyngby, Denmark.*

³⁾ *Department of Chemistry, Norwegian University of Science and Technology, N-7491 Trondheim, Norway.*

⁴⁾ *Dipartimento di Chimica e Tecnologia dei Farmaci, Università degli Studi di Roma “La Sapienza”, piazzale Aldo Moro 5, I-00185 Rome, Italy.*

⁵⁾ *CNR - Istituto Officina dei Materiali (IOM), Laboratorio TASC, 34149 Trieste, Italy.*

(Dated: 24 February 2026)

We report a combined experimental and computational study of the near-edge X-ray absorption fine structure (NEXAFS) spectrum of the propargyl radical, $C_3H_3 \cdot$. As a central intermediate in the formation of polycyclic aromatic hydrocarbons, the propargyl radical is a species of considerable relevance in combustion and astrochemistry and was here generated by pyrolysis from propargyl bromide. The NEXAFS spectrum shows a pronounced band at 282.2 eV corresponding to transitions from carbon 1s orbitals to singly occupied molecular orbitals. *Ab initio* calculations show that two transitions to the lowest lying states 1^2A_1 and 2^2A_1 , which take place from the C1s orbital of the two terminal carbon atoms, contribute to this band. In addition, a 420 meV spacing of the first band is visible and is assigned to a vibrational progression in the symmetric CH_2 stretch. Transitions at higher energies are also described reasonably well by theory. The fragmentation pattern was investigated at the different resonant transitions and shows the cleavage of one as well as both C–C bonds.

Keywords: propargyl, NEXAFS, X-ray spectroscopy, computation, carbon edge

I. INTRODUCTION

The mechanism of the formation of polycyclic aromatic hydrocarbons (PAHs) is a major research topic in astrochemistry as well as in combustion science.^{1–4} In interstellar space, PAHs and their cations are investigated as possible carriers of the diffuse interstellar bands (DIB) as well as the unidentified infrared bands (UIB).⁵ They have been postulated to comprise a significant part of the carbon budget in space.⁶ However, the formation mechanism of PAHs in the low pressure and low temperature environment of space is an open question.³ Barrierless or low-barrier reactions, such as ion-molecule and radical-radical reactions, offer a possible explanation. In combustion, the dimerization of propargyl, $C_3H_3 \cdot$, was found to be an efficient reaction that proceeds in a sequence of barrierless steps to benzene and phenyl radical.^{7,8} Propargyl, shown on the right-hand side of Scheme 1, is a resonantly stabilized radical of C_{2v} symmetry with a \tilde{X}^2B_1 ground state.⁹ For the nominal resonance structures ethynyl methyl ($H_2C \cdot - C \equiv CH$) and allenyl ($H_2C = C = C \cdot H$), a ratio of 61% to 39% was inferred from recent microwave measurements analyzing the spatial distribution of the unpaired electron.¹⁰ Propargyl is a well-known intermediate in flames and plasmas and has

recently been detected in the cold dark Taurus Molecular Cloud (TMC-1)^{11,12} where the corresponding cationic species has been observed as well.¹³ The detection was based on prior laboratory microwave spectra.¹⁴ It was suggested that propargyl is “one of the most abundant radicals detected in TMC-1, and it is probably the most abundant organic radical with a certain chemical complexity ever found in a cold dark cloud.”¹¹ Most likely, it is also involved in the atmospheric chemistry of the Saturn moon Titan.¹⁵ Given its abundance, the propargyl radical may be involved in the synthesis of aromatic molecules in space as well. For example, the ion-molecule reaction $H_2CCCH \cdot + C_3H_3^+ \rightarrow C_6H_5^+ + H \cdot$ has been suggested to be an efficient source for formation of the phenyl cation.¹⁶ Due to the importance of the propargyl radical in astrochemistry and in combustion chemistry, its spectroscopy and chemistry have been broadly investigated. Specifically, infrared,^{17,18} UV/Vis^{19,20} and photoelectron spectra,^{21–23} including a study that followed the steps to benzene formation,²⁴ have been reported. The photodissociation has been studied by H-atom photofragment spectroscopy,²⁵ high Rydberg atom time-of-flight (HRTOF) spectroscopy,²⁶ and in a Laval nozzle expansion.²⁷ Hydrogenation reactions of $C_3H_3 \cdot$ and related cations important for carbon chemistry in space have been studied in ion traps.^{28,29} The bimolecular recombination of propargyl was studied in the gas-phase and branching ratios of the isomeric C_6H_6 reaction products were determined.^{30,31} The further efficient growth of PAHs by a subsequent addition

^{a)} E-mail: ingo.fischer@uni-wuerzburg.de (experiment)

^{b)} E-mail: socio@kemi.dtu.dk (theory)

of propargyl units to the first ring has been investigated by IR/UV ion dip spectroscopy.³² Both the structure as well as reactions of the propargyl radical have also been investigated computationally, with a focus on the propargyl dimerization.^{9,33} Possible mechanisms for PAH formation and growth reactions that include propargyl as one reactant have been studied experimentally^{34–37} and computationally.^{38–40} Propargyl has also been investigated as precursor for polycyclic aromatic nitrogen containing heterocycles (PANH) formation in space.⁴¹

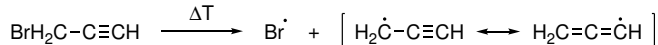
In contrast to the investigations in other spectral regions, the response of polyatomic organic radicals to X-ray excitation has hardly been studied. The astrochemical relevance of this topic originates from the X-ray emission in young stellar objects that might have a significant influence on the circumstellar molecular composition.⁴² So far, X-ray absorption near the first C1s ionization threshold (XAS, NEXAFS) in hydrocarbon radicals has only been investigated for allyl, $C_3H_5^\bullet$,⁴³ methyl, CH_3^\bullet ,⁴⁴ and its isotopomer CD_3^\bullet ,⁴⁵ as well as *tert*-butyl, $C_4H_9^\bullet$.⁴⁶ A recent study focused on the C1s NEXAFS spectroscopy of different isomeric $C_3H_3^+$ cations, including the propargylium ion. There, site-specific resonances and fragmentation channels leading to doubly charged fragments were investigated.⁴⁷

In the present work, we address the NEXAFS spectroscopy of neutral propargyl, one of the astrochemically most important radicals, in a combined experimental and computational study. This work will also help to identify the propargyl radical in future studies using time-resolved X-ray spectroscopy.

II. METHODS

A. Experimental

The experiments were carried out at the Gas Phase Photoemission beamline at the Elettra Synchrotron, Trieste/IT. The setup has been detailed previously,^{48,49} but a brief description is given in the following. Synchrotron light at the C1s edge and at 21.2 eV was provided by an undulator and spectrally dispersed by a variable angle, spherical grating type monochromator. Different gratings were used for different photon energy regions, and the photon energy resolution was controlled by the entrance and exit slit width.



Scheme 1. Generation of the propargyl radical, H_2CCCH^\bullet , by pyrolysis of propargyl bromide. On the right-hand side the ethynyl methyl and allenyl resonance structures of the propargyl radical are shown.

The precursor propargyl bromide (stabilized with MgO) was purchased from TCI and used after several freeze-pump-thaw cycles. The precursor was cooled to

−30 °C, and the vapor of the precursor diluted in helium (dilution of 0.1 %) passed through a resistively heated SiC pyrolysis tube. Scheme 1 shows the pyrolysis of propargyl bromide that yields the propargyl radical and a bromine atom.^{21,25} The pyrolysis products were expanded into the vacuum and entered the experimental chamber through a skimmer. The molecular beam was crossed by the synchrotron radiation, and the resulting electrons and ions were extracted in opposite directions. Electrons and ions were detected in coincidence by a single start-multiple stop technique. The electrons were detected by an MCP detector, set close to the ionization region, and used as start signal for the ion time-of-flight (TOF). Ions were detected by a Wiley-McLaren TOF mass spectrometer.

The pyrolytic conversion of the precursor according to Scheme 1 was investigated by valence photoionization mass spectrometry at 21.2 eV. For C1s NEXAFS spectra the total electron yield (TEY) was recorded while the photon energy was scanned. The photon flux was monitored by a photodiode and used for normalization of the spectra. To correct for the helium background in the spectra, a spectrum of pure helium was measured and subtracted. In a diagnostic chamber in front of the experimental chamber, methane was measured simultaneously to calibrate the photon energy by its C1s → 3p-Rydberg transition at 288.00 eV.⁵⁰ The photon bandwidth around the C1s edge was 50 meV. The C1s NEXAFS spectra in the region 280.3–297.2 eV were measured with a step size of 20 meV and an acquisition time of 45 s (pyrolysis at 35 W heating power) and 35 s (pyrolysis off) per data point. High-resolution spectra in the range 281.3–283.3 eV were measured with a step size of 10 meV and an acquisition time of 75 s. Valence photoionization mass spectra at 21.2 eV were recorded with acquisition times between 300 s and 1800 s, while mass spectra at the C1s edge were acquired for 6000 s.

B. Computational

Two *ab initio* electronic-structure approaches were adopted for the computational study of the electronic transitions, namely the frozen-core core-valence-separated equation-of-motion coupled cluster singles and doubles (fc-CVS-EOM-CCSD) method,⁵¹ and the extended core-valence-separated second-order algebraic diagrammatic construction (CVS-ADC(2)-x) method,⁵² as implemented in Q-Chem.⁵³ A preliminary basis set study was performed at the fc-CVS-EOM-CCSD level using both restricted-open (ROHF) and unrestricted (UHF) Hartree-Fock reference orbitals, and the 6-311++G**,^{54–56} cc-pVTZ,⁵⁷ and aug-cc-pVTZ⁵⁸ basis sets on all atoms. Unrestricted Hartree-Fock reference orbitals and the aug-cc-pVTZ basis set were adopted at the CVS-ADC(2)-x level. Core ionization energies were obtained at the fc-CVS-EOM-IP-CCSD level.

We used the CCSD(T*)-F12a^{59,60}/cc-pVTZ-F12⁶¹-optimized molecular geometry (planar C_{2v} structure)

from Botschwina and Oswald⁹ in all calculations of the purely electronic spectra. This structure is rather similar to the recently reported semi-experimental equilibrium geometry of Changala *et al.*¹⁰ The bond lengths of both structures are reported in Table S8 in the SI. As observed by the authors of Ref. 10, the deviation of the C–C bond lengths in the ground state of propargyl from pure single, double and triple bonds are “[...] evidence of π -delocalization of the unpaired electron along the carbon backbone”.

Natural transition orbitals (NTOs)^{51,62} were computed at the corresponding fc-CVS-EOM-CCSD and CVS-ADC(2)-x levels of theory and used for the assignment of the spectral peaks. The spectra were constructed from the computed excitation energies and oscillator strengths using a Lorentzian convolution with a full width at half maximum (FWHM) broadening of 200 meV. All calculations were carried out on DTU HPC resources.⁶³

Three different strategies were adopted to investigate vibrational effects in the spectrum. In the first strategy, the nuclear ensemble approach (NEA),⁶⁴ we sampled 200 vibrational structures of the ground state using a Wigner sampling at a temperature of 300 K. The ground state frequencies used for sampling the vibrational structures are calculated from a B3LYP⁶⁵/aug-cc-pVTZ optimized geometry. For all structures the NEXAFS spectrum was then calculated using both fc-CVS-EOM-CCSD and CVS-ADC(2)-x with the aug-cc-pVTZ basis set. In the second and third strategy, both a time-independent (TI) and a time-dependent (TD) quantum approach were utilized for the calculation of the vibrational structure of the selected electronic transitions in the NEXAFS spectrum.^{66,67} The (eigenstate-free) TD approach delivers directly the vibrationally resolved spectral profile, whereas the TI approach is based on the individual stick transitions of all possible vibronic states, which are then broadened. The potential energy surfaces (PES) associated with the electronic states involved in the transition that are required by both methods were obtained from the harmonic Vertical Gradient (VG)^{66,68,69} and Adiabatic Shift (AS)^{66,69} approximations, respectively. `FCclasses3`⁶⁷ was used for these calculations. The VG and AS approximations both utilize the ground state energy, gradient, and Hessian as well as the excitation energy and a 1-norm dipole moment along the same direction (x , y , and z) as the transition dipole moment. The two methods differ in the way they treat the excited state geometry and gradient when reconstructing the PES of the final electronic state.⁶⁶ For the VG approximation (also known as linear coupling model⁶⁸), the ground state geometry is used also for the excited state, and the excited state gradient is calculated at this geometry. In the AS approximation, the excited state geometry is optimized, and the excited state gradient is practically zero within the chosen optimization threshold. The ground and excited state(s) share the same normal modes and frequencies, as the same Hessian is used for both.⁶⁶ The spectra are scaled afterwards using

the transition dipole strength. We used a UMP2/aug-cc-pVDZ optimized geometry from Gaussian⁷⁰ followed by excited state geometry optimizations at the ADC(2)-x level for the first three bright states using PySCF^{71,72} for the Hartree-Fock calculation, ADCC⁷³ for the excitation energy calculation, `cvs-adc-grad`⁷⁴ for the excited state gradient, and `geomeTRIC`⁷⁵ for the excited state geometry optimization. The vibrationally resolved spectral bands were broadened by a Voigt function with a Gaussian FWHM of 50 meV and a Lorentzian FWHM of 100 meV, corresponding to the experimental photon bandwidth and the approximate lifetime width of the C1s core hole, respectively. We computed both TI and TD spectra at 0 K, as well as TD ones at 300 K. We refer to Section S2.1 in the Supplementary Information (SI) for additional computational details.

III. RESULTS AND DISCUSSION

A. Experimental NEXAFS spectrum

Figure 1 shows the comparison of the valence photoionization mass spectrum without pyrolysis (upper trace, a) and with optimized pyrolysis conditions (lower trace, b). The spectra were recorded at 21.2 eV to confirm the pyrolytic conversion of the precursor according to scheme 1. Both spectra were normalized to the mass signal of the carrier gas helium at m/z 4. Without pyrolysis the parent ion of the precursor, $C_3H_3Br^+$, is observed at m/z 118 and 120 with a double peak structure originating from the two isotopes ⁷⁹Br and ⁸¹Br. Dominant signals at m/z 39, 38, and a weaker one at m/z 37 result from the dissociative photoionisation (DPI) of the precursor to $C_3H_3^+$, $C_3H_2^+$ and C_3H^+ . For $C_3H_3^+$ an appearance energy of 10.88 eV was determined previously,⁷⁶ and also C_3H^+ was formerly identified as a DPI product of the precursor in spectra taken at 15.77 eV.⁷⁷ Measurements with pyrolysis were performed at a power of 35 W, corresponding to a SiC capillary temperature of approximately 1200 °C. The radical, which has a rich vibrational manifold of states with many low frequency vibrational modes, is assumed to be in the interaction region vibrationally cold, due to the efficient adiabatic expansion in the jet source. The corresponding mass spectrum in Figure 1b) shows new bromine signals from the pyrolysis and only a negligibly small $C_3H_3Br^+$ mass signal of the unpyrolysed precursor. The peak at m/z 39 is lower in intensity and narrower compared to the spectrum of the pure precursor and is likely to belong both to the pyrolytically generated propargyl radical $C_3H_3^+$ and to the DPI product of the unconverted precursor. The latter shows a broad pedestal below this peak, which results from the kinetic energy release in the DPI. Compared to the pure precursor spectrum the relative intensity of both $C_3H_2^+$ and C_3H^+ to $C_3H_3^+$ is increased. $C_3H_2^+$ and C_3H^+ are known DPI products of the propargyl radical that are associated with appearance energies of 12.5–13 eV and

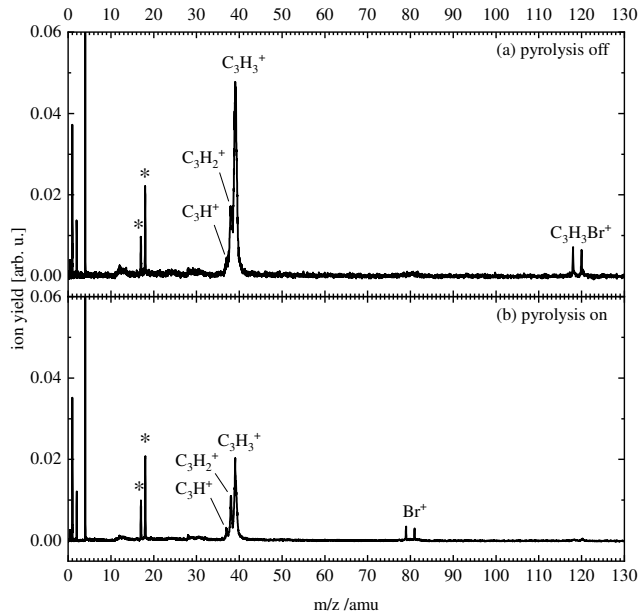
>15.5 eV.⁷⁷

FIG. 1. TOF mass spectra at 21.2 eV with (a) pyrolysis off and (b) pyrolysis on. The spectra were normalized to the He⁺ signal at m/z 4. Asterisks indicate water as impurity.

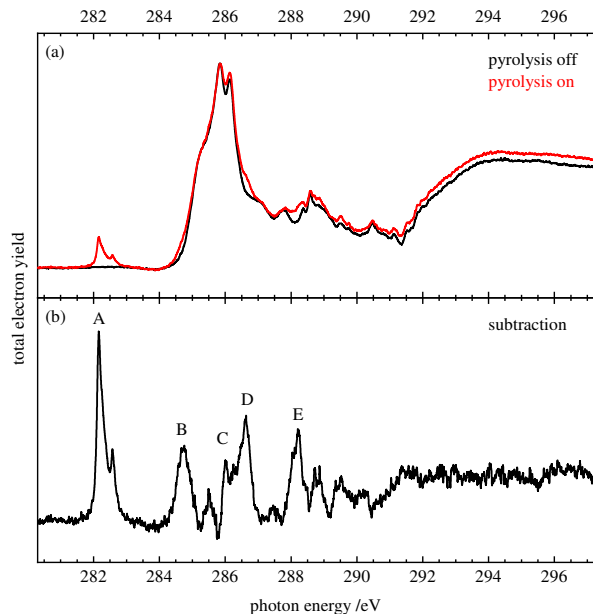


FIG. 2. (a) C1s NEXAFS spectra of the precursor propargyl bromide without and with pyrolysis. (b) C1s NEXAFS spectrum of the propargyl radical obtained from subtraction.

NEXAFS spectra at the C1s edge were recorded as TEY with and without pyrolysis and are shown in the upper trace of Figure 2. The spectrum of the precursor (black line) sets in above 284 eV and shows an intense signal around 286 eV with a double peak structure with a spacing of 300 meV. At higher photon energies several

less intense signals are observed, and the TEY increases above 291 eV, when the C1s ionization thresholds are approached. The absorption spectrum with pyrolysis (red line) corresponds to the spectrum of the precursor and the propargyl radical. A new band is found at 282.2 eV and its shift to much lower photon energies compared to the pure precursor is a fingerprint of an open shell species. It is attributed to a transition from a C1s orbital into a singly occupied molecular orbital (SOMO) of the unpaired electron of the propargyl radical (section III B). The spectrum of the pure radical was obtained by subtraction of the spectra with and without pyrolysis where the onset and the maximum of the band at 286 eV were used to scale the spectrum of the pure precursor. The resulting spectrum of the propargyl radical is shown in Figure 2(b). Band A that corresponds to the transition into the SOMO shows a vibrational progression of 420 meV. A broad structureless feature is found at 284.8 eV (B), which is red-shifted with respect to the main signal of the precursor. In contrast, signals at 286.0 eV (C), 286.6 eV (D) and 288.2 eV (E) correspond to new signals at the maximum or the high energy flank of the precursor's main signal and are visible from Figure 2(a).

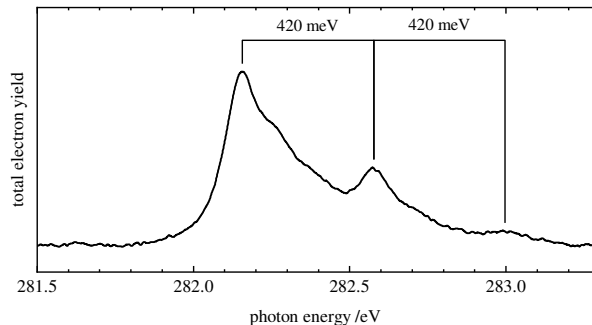


FIG. 3. High resolution NEXAFS spectrum of the C1s to SOMO transition (band A).

To investigate the vibrational structure of the lowest band in the propargyl spectrum, band A was scanned with a smaller step size and is displayed in Figure 3. A progression with three components was identified. The spacing of 420 meV suggests the excitation of a C–H stretching vibration upon the C1s to SOMO excitation. The first component at 282.16 eV (and possibly also the second one at 282.58 eV) also reveals a high-energy shoulder that may belong to a simultaneously excited bending vibration. To understand how electronic and/or vibrational excitations influence the appearance of this first band (A), a theoretical assignment of the spectrum is indispensable.

B. Computational results and spectral assignment

For the computational discussion, we denote the CH₂ carbon of the propargyl radical as C1 and the CH as C3,

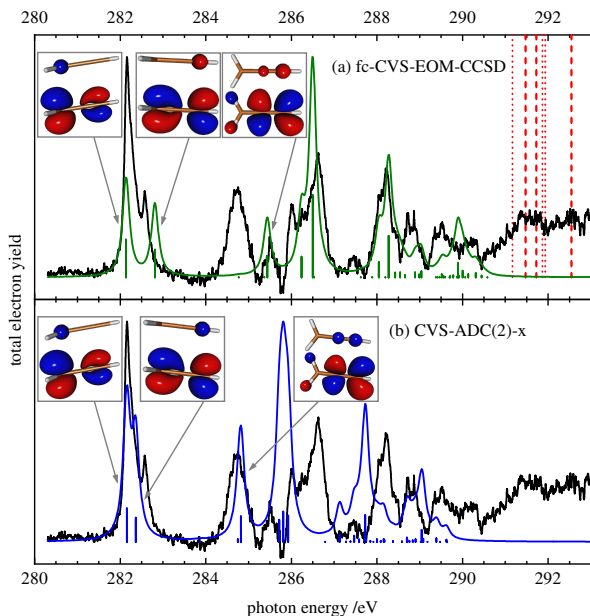


FIG. 4. Comparison between experimental NEXAFS spectrum (black line) and computed (a) fc-CVS-EOM-CCSD/aug-cc-pVTZ and (b) CVS-ADC(2)-x/aug-cc-pVTZ NEXAFS spectra of the propargyl radical using UHF reference orbitals. The sticks were convoluted with a Lorentzian lineshape function with a FWHM of 200 meV. The vertical red dashed lines are the fc-CVS-EOM-IP-CCSD ionization potentials to singlet ionic states and the dotted ones to triplet ionic states.

with the carbon in between as C2. The bands in Figure 2 are assigned based on *ab initio* calculations at the fc-CVS-EOM-CCSD and CVS-ADC(2)-x levels of theory using the aug-cc-pVTZ basis set. All computed excitation energies and their associated oscillator strengths are summarized in Table S3 of the SI. Additional fc-CVS-EOM-CCSD results obtained with other basis sets are collected in Table S4. NTOs are given in Tables S5 and S6, for fc-CVS-EOM-CCSD and CVS-ADC(2)-x, respectively. The corresponding simulated spectra are shown in Figures S2 and S3. A comparison of the simulated spectra in Figure S2 shows that a change in basis set leads to a shift in the spectrum when compared to the experimental results and the splitting of the first two transitions narrows when changing from an open-shell restricted to an unrestricted Hartree-Fock reference. Overall, the fc-CVS-EOM-CCSD spectral profiles are rather similar.

Comparing the unrestricted fc-CVS-EOM-CCSD/aug-cc-pVTZ spectrum to the CVS-ADC(2)-x/aug-cc-pVTZ one in Figure 4, we note that the energy separation of the first two transitions narrows further at the CVS-ADC(2)-x level, and the third transition shifts in position and increases in intensity, overlapping with the experimental band B at 284.8 eV.

Based on the computed spectral data and NTOs, band A at 282.2 eV is assigned to a combination of the transitions to the 1^2A_1 state ($C1\ 1s \rightarrow \text{SOMO}$) and to the

2^2A_1 state ($C3\ 1s \rightarrow \text{SOMO}$). These are located at 282.15 eV and 282.36 eV, respectively, by CVS-ADC(2)-x, and at 282.13 eV and 282.81 eV by fc-CVS-EOM-CCSD. We note that the SOMO particle NTO is of (ethynyl methyl) $p(C1)-\pi(C2-C3)$ character for the transition to the 1^2A_1 state, and of (allenyl) $\pi(C1-C2)-p(C3)$ character for the transition to the 2^2A_1 state. This is suggestive of the core excitation taking place from either an ethynyl methyl or an allenyl resonance structure (compare Scheme 1).

The experimental band B at 284.8 eV overlaps with the CVS-ADC(2)-x transition to the 2^2A_2 state at 284.82 eV, which consists of a core excitation from the 1s orbitals of C2 and C3 to an in-plane π^* orbital (suggesting the presence of a triple bond between C2 and C3, as expected in the nominal ethynyl methyl resonance structure). The third transition in the fc-CVS-EOM-CCSD calculation is less intense and located at higher energy than the experimental band B (overlapping with the less intense peak at its right) but has the same character as the CVS-ADC(2)-x one.

Moving towards the region of bands C–D of the experimental spectrum (286.0–286.6 eV), we note that CVS-ADC(2)-x yields three dipole allowed transitions with sizable intensity, whereas fc-CVS-EOM-CCSD gives only two. In both cases, our computed transitions are slightly too closely spaced, yielding a narrower and more intense band when convoluted. Above 285.5 eV, the CVS-ADC(2)-x transitions are also more red-shifted than the fc-CVS-EOM-CCSD ones, and do not overlap well with the experimental bands. Nonetheless, the C–D region of the experimental spectrum is dominated, according to our calculations with both methods, by transitions from the C2 1s orbital (with some mixing of the C3 one) to either the in-plane or the out-of-plane π^* particle NTOs (shown in Table S5 and S6).

As for the band E just above 288 eV in the experimental spectrum, several transitions, some with rather low intensity, contribute. At fc-CVS-EOM-CCSD level, two transitions are most intense, with the strongest one at 288.28 eV due to a $C2\ 1s \rightarrow (\text{out-of-plane})\ \pi^*$. Similarly, several transitions contribute to the band E at CVS-ADC(2)-x level, with the most intense one at 287.73 eV (again red-shifted compared to experiment), and the same character as the intense E transition from fc-CVS-EOM-CCSD.

We also computed core ionization energies for all three carbon atoms by the fc-CVS-EOM-IP-CCSD approach, summarized in Table S2 and given as red vertical lines in Figure 4. For the formation of a singlet cation, the lowest ionization energy of 291.5 eV was found for the acetylenic carbon (C3), and the value of the central carbon is only slightly higher by 0.1 to 0.2 eV. For the C1 carbon, the highest value of 292.6 eV was found. The ionization energy value for the formation of a triplet cation is found to be higher than the one of the singlet state for C2, while the reverse is observed for the terminal carbon atoms.

To conclude this section, we return to the first elec-

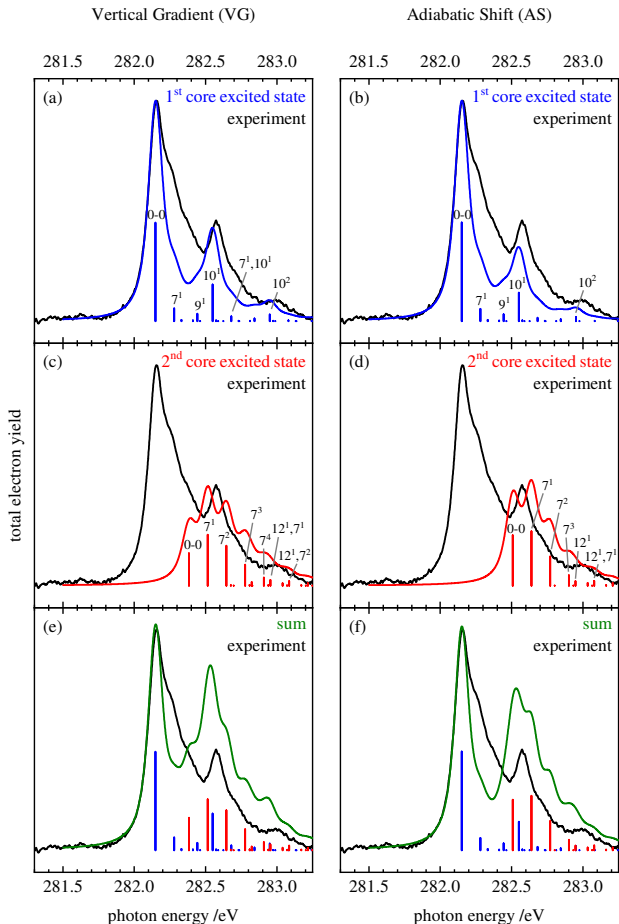


FIG. 5. Comparison between the high-resolution experimental NEXAFS spectrum (black line) and vibrational structure of the (a, b) first, (c, d) second and (e, f) sum of both first and second CVS-ADC(2)-x electronic transitions at 0 K, with PES obtained from the Vertical Gradient (left) and Adiabatic Shift (right) approximations. Vertical lines show the vibronic stick transitions from the vibrational ground state in the initial electronic state obtained using the time-independent formalism.⁶⁶ The labels correspond to the vibrational state in the final electronic states, represented as X^v , where X is the normal mode index and v is the number of quanta. All VG results have been shifted by +175 meV and all AS ones by +318 meV to align with the first experimental peak. The spectra have been scaled such that the intensity of the 0-0 band of the first electronic transition overlaps with experiment.

tronic transitions associated to band A, and discuss the results of our calculations of its vibrational structure. The Wigner samplings shown in Figure S5 indicate a vibrational splitting of the A band. This splitting becomes even more evident in the vibrationally resolved spectra that were obtained from the TI calculations based on the VG and AS potential energy surfaces and that are shown in Figure 5 for CVS-ADC(2)-x. The TD calculations for both fc-CVS-EOM-CCSD and CVS-ADC(2)-x are presented in Figure S4.

Figure 5(a) and (b) show that the first electronic transition has a vibrational splitting (three bands) consist-

ent with the experimental results. Assignment of which vibronic transitions contribute to each vibrationally resolved band can be done based on the stick transitions from the TI results (with labels X^v , where X indicates the mode involved and v the amount of quanta in the mode). The most intense band at 282.16 eV is dominated by the 0-0 transition, with a smaller contribution from the transition from the $v = 0$ level of the electronic ground state to the 7^1 vibrational state of the core excited state. The second band of the progression at 282.58 eV is dominated by the 10^1 vibrational state of the core excited state, with a smaller contribution from 9^1 . The third band is mainly 10^2 , i.e., a two-quanta vibrational state transition of mode 10. As summarized in Table S7 (and Figure S8), normal mode 10 is the symmetric CH_2 stretching (of C1), mode 7 is dominated by the C1-C2 stretching and mode 9 by the C2-C3 stretching. Inclusion of temperature effects in the TD treatment does not seem to have any visible effect, see Figures S6-S7, which is not surprising giving the level of approximation used for the vibrational calculations.

The vibrationally resolved spectrum of the second electronic transition shown in Figure 5(c) and (d) is an asymmetric band that overlaps with the 10^1 band of the first electronic transition. The band is not peaked at the 0-0 transition, but rather at the 7^1 transition, and with its additional quanta $v = 2, 3, 4$ and 5 (together with some excitation of mode 12, which is the C3-H stretch) contributing to its long tail. The sum of the spectra of both the first and second electronic state in Figure 5(e) and (f) indicates that the overall intensity of the band at 282.58 eV is overestimated. According to our calculations, the ratio of the oscillator strengths between the first and second excited states is 0.58:0.42. This shows a similar trend for the two nominal resonance structures as the 0.61:0.39 ratio found in the recent study by Changala *et al.*¹⁰ The dominant excitation of vibrational mode 10 (symmetric CH_2 stretch of C1) and of mode 7 (C1-C2 stretch) upon transition into the first and second core excited state, respectively, can be related to the change in the molecular geometry upon the C1s excitation. Comparing the structure of the ground state with those of the lowest core excited states (given in Table S8), we note that for the first electronic transition the strongest geometry change is the reduction of the C1-H bond length, and of the C1-C2 bond length upon excitation of the second electronic transition.

From these results, we conclude that the splitting of band A in the experimental spectrum mainly results from the vibrational structure of the first electronic transition (from the ethynyl methyl radical form), specifically the 0-0 transition and the symmetric stretching of the two C1-H bonds, possibly with contributions from the vibrational structure of the second electronic transition (allenyl radical form), due to 0-0 and 7^v transitions ($v = 1 - 5$), with some participation of mode 12, too.

C. Comparison of the propargyl and allyl radical

As both propargyl ($C_3H_3^{\bullet}$) and allyl ($C_3H_5^{\bullet}$) are resonance-stabilized hydrocarbon radicals, it is worth to briefly compare their NEXAFS spectra. Both radicals are characterized by a terminal $C1s \rightarrow SOMO$ transition at around 282 eV. The presence of a transition shifted to lower photon energies compared to closed-shell molecules is a characteristic of radicals and has also been observed for the *tert*-butyl radical.⁴⁶ In fact, also the shape of band A at 282.2 eV resembles one of the lowest-energy core excitation of the allyl radical, which was observed at 281.99 eV,⁴³ and shows a progression that was assigned to a combination of a C–H stretch and an out-of-plane bending mode. However, as the terminal carbon atoms are equivalent in allyl (two equivalent resonance structures), the band is somewhat simpler, as it can be described by a single electronic transition (whereas two electronic transitions contribute to band A of propargyl). In addition, its NEXAFS spectrum shows fewer bands. However, transitions B–E in Figure 2 can be related to the central and terminal $C1s$ to LUMO transitions in allyl that were observed at 285.27 eV, 285.71 eV and 287.50 eV.⁴³

D. Fragmentation after core excitation

After the resonant core excitation, the core excited states decay via Auger-Meitner processes. The resulting ions were detected by TOF mass spectrometry, and the coincidence setup was used to differentiate between ions from single, double or triple ion events. The fragmentation of the propargyl radical after $C1s \rightarrow SOMO$ excitation was investigated at 282.2 eV (band A). Figure 6 shows the corresponding mass spectrum for single ion events that was corrected for contributions from off-resonant excitation and unpyrolyzed precursor contributions. The observed fragments and their branching ratios are summarized in Table I.

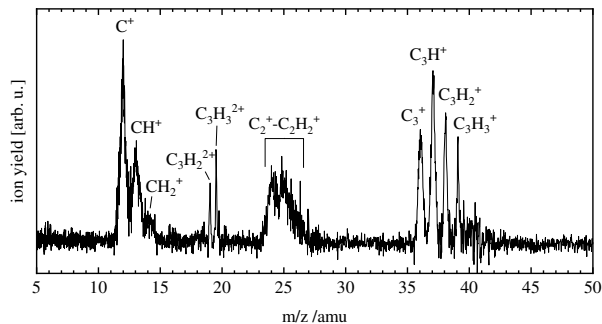


FIG. 6. TOF mass spectrum of single ion events upon excitation of the propargyl radical at band A at 282.2 eV ($C1s \rightarrow SOMO$).

The parent ion $C_3H_3^+$ is observed as a sharp signal at m/z 39. Signals at m/z 38, 37 and 36 result from a loss of

TABLE I. Branching ratios of single ion events after excitation of the propargyl radical at 282.2 eV (band A). Relative intensities were determined from the mass spectrum (Figure 6) by integration. Integrals of overlapping masses were derived from fitting with Gauss functions. The branching ratios were normalized so that all channels sum up to 100%. Very low branching ratios are not specified and are summarized in “others”. The error of each branching ratio is estimated to be around $\pm 20\%$ of the respective branching ratio.

m/z	species	branching ratio /%
39	$C_3H_3^+$	4
38	$C_3H_2^+$	8
37	C_3H^+	13
36	C_3^+	10
26	$C_2H_2^+$	6
25	C_2H^+	12
24	C_2^+	9
19.5	$C_3H_3^{2+}$	2
19	$C_3H_2^{2+}$	–
14	CH_2^+	4
13	CH^+	13
12	C^+	17
6	C^{2+}	–
others		2

neutral hydrogens. The signals at m/z 19.5 and 19 belong to the dications $C_3H_3^{2+}$ and $C_3H_2^{2+}$ that are produced by double Auger decay. Most of the fragmentations include the cleavage of one (27%) or both (34%) carbon-carbon bonds. Mass signals for $C_2H_2^+$ to C_2^+ and CH_2^+ to C^+ are broader because of the kinetic energy released in the fragmentation. The absence of C_1 or C_2 fragments carrying three hydrogens in the mass spectrum leads us to conclude that no rearrangement of the hydrogen atoms to the higher-energy isomer 1-propenyl cation, $[H_3C-C-C]^+$,⁴⁷ takes place in the cationic state. For this isomer the detection of $C_2H_3^+$ or CH_3^+ would have been expected. However, we cannot exclude an isomerisation to the lower-energy cyclopropenyl, $C_3H_3^+$, on the cationic surface based on our mass spectrometric data.

We also investigated excitations into higher core excited states at 286.0 eV (band C), 286.6 eV (band D) and 288.1 eV (band E). The corresponding mass spectra and branching ratios can be found in Section S1 in the SI. Compared to the $C1s \rightarrow SOMO$ transition these excitations show a stronger fragmentation tendency with less C_3 fragments. This is like our previous observations for the *tert*-butyl radical and was explained by a preference for spectator decay over participator decay for higher excitation energies.⁴⁶

IV. CONCLUSION

The NEXAFS spectrum of the propargyl radical at the $C1s$ edge has been recorded using synchrotron radiation. The radical was generated by pyrolysis of propargyl bro-

mide. Although the radical is converted cleanly, conversion of the precursor was not complete and the spectrum of propargyl bromide had to be subtracted. Upon pyrolysis, a new feature emerges at 282.2 eV that is due to C1s \rightarrow SOMO transitions. By comparison with CVS-ADC(2)-x and fc-CVS-EOM-CCSD computations, it was found that two core-excited states ($1\ ^2A_1$ and $2\ ^2A_1$) contribute to this band, the first originating from the excitation of a 1s electron from the terminal C1 atom into a SOMO of ethyl allenyl character, and the second from the excitation of a 1s electron from the terminal C3 atom into a SOMO of allenyl character. Our results are consistent with those of a recent study using hyperfine-resolved microwave spectroscopy and accurate *ab initio* computations,¹⁰ indicating that propargyl possesses a π -delocalized resonance structure of intermediate ethynyl methyl and allenyl character, with non-equal 0.61:0.39 balance between the relative weights of the two resonance structures.

This first band at 282.2 eV exhibits a vibrational progression with a spacing of 420 meV. By means of vertical and adiabatic harmonic calculations, this is mainly assigned to the symmetric CH₂ stretching mode of the first core-excited state (C1 1s \rightarrow SOMO of ethynyl methyl), possibly with contributions from the vibrational structure of the second core excited state (C3 1s \rightarrow SOMO of allenyl). In addition, several bands at higher photon energy can be assigned to transitions from C2 and C3 into the π^* orbitals. Overall, the appearance of the spectrum resembles the one of the allyl radical, C₃H₅ \cdot .

Core ionization energies between 291.5 eV and 292.6 eV for ionization into the singlet cation were computed for the different carbon atoms. Compared to the singlet cation, the ionization energy into the triplet cation is lower for the two terminal C atoms, but is slightly higher for the central one.

The fragmentation pattern upon (terminal) C1s \rightarrow SOMO excitation shows peaks of the molecular cation and dication, but also a broad distribution of fragments including loss of one to three H-atoms, and cleavage of one or both C–C bonds. Interestingly, no CH₃⁺ is observed, indicating the absence of isomerization to propenyl. In comparison, excitation to higher core-excited states is associated with a more pronounced fragmentation dominated by the almost complete disappearance of the molecular cation and an increasing dominance of C₁⁺ fragment ions.

V. SUPPLEMENTARY MATERIAL

See supplementary information for mass spectra at higher photon energies, additional computational details and results.

VI. ACKNOWLEDGMENTS

The work has been financially supported by the German Science Foundation (DFG), contract FI 575/13-2. D.S. acknowledges a fellowship by the Fonds der Chemischen Industrie (FCI). We acknowledge invaluable discussions with Dr. Fabrizio Santoro and Dr. Iulia Emilia Brumboiu. J.P. acknowledges financial support from the Technical University of Denmark within the Ph.D. Alliance Programme. S.C. thanks Hamburg’s Cluster of Excellence “CUI: Advanced Imaging of Matter” for the 2024 Mildred Dresselhaus Prize. S.C. and T.J.v.B. acknowledge funding from the Novo Nordisk Foundation (NNF Grant No. NNFSA220080996). S.S. and A.B. acknowledge financial support from the University of Rome “La Sapienza”, project Ateneo 2024 RG1241909C0A0A47, and a PhD fellowship, respectively.

DATA AVAILABILITY STATEMENT

The data are available from the authors upon reasonable request.

VII. AUTHOR CONTRIBUTIONS

D.S., A.R., E.K., V.v.L., A.B., M.A., S.S., and I.F. designed and conducted the experiments. T.J.v.B., J.P. and S.C. designed the computational protocols, carried out the calculations and characterized the NEXAFS spectra based on the *ab initio* results. D.S. analyzed the experimental data and wrote the first draft of the paper; T.J.v.B. and S.C. wrote the parts concerning the computational results. All authors discussed the interpretation of the results and contributed to the final version of the paper.

REFERENCES

- ¹H. Richter and J. Howard, “Formation of polycyclic aromatic hydrocarbons and their growth to soot—a review of chemical reaction pathways,” *Prog. Energy Combust. Sci.* **26**, 565–608 (2000).
- ²M. E. Kress, A. G. Tielens, and M. Frenklach, “The ‘soot line’: Destruction of presolar polycyclic aromatic hydrocarbons in the terrestrial planet-forming region of disks,” *Adv. Space Res.* **46**, 44–49 (2010).
- ³Z. D. Levey, B. A. Laws, S. P. Sundar, K. Nauta, S. H. Kable, G. da Silva, J. F. Stanton, and T. W. Schmidt, “PAH Growth in Flames and Space: Formation of the Phenalenyl Radical,” *J. Phys. Chem. A* **126**, 101–108 (2022).
- ⁴A. N. Byrne, C. Xue, I. R. Cooke, M. C. McCarthy, and B. A. McGuire, “Astrochemical modeling of propargyl radical chemistry in TMC-1,” *ApJ* **957**, 88 (2023).
- ⁵A. G. G. M. Tielens, “The molecular universe,” *Rev. Mod. Phys.* **85**, 1021–1081 (2013).

- ⁶A. G. G. M. Tielens, "Interstellar polycyclic aromatic hydrocarbon molecules," *Annu. Rev. Astron. Astrophys.* **46**, 289–337 (2008).
- ⁷U. Alkemade and K.-H. Homann, "Formation of C₆H₆ Isomers by Recombination of Propynyl in the System Sodium Vapour/Propynylhalide," *Z. Phys. Chem., Neue Folge* **161**, 19–34 (1989).
- ⁸S. E. Stein, J. A. Walker, M. M. Suryan, and A. Fahr, "A new path to benzene in flames," *Symp. (Int.) Combust.* **23**, 85–90 (1991).
- ⁹P. Botschwina and R. Oswald, "Calculated photoelectron spectra of isotopomers of the propargyl radical (H₂C₃H): An explicitly correlated coupled cluster study," *Chem. Phys.* **378**, 4–10 (2010).
- ¹⁰P. B. Changala, P. R. Franke, J. F. Stanton, G. B. Ellison, and M. C. McCarthy, "Direct Probes of π -Delocalization in Prototypical Resonance-Stabilized Radicals: Hyperfine-Resolved Microwave Spectroscopy of Isotopic Propargyl and Cyanomethyl," *J. Am. Chem. Soc.* **146**, 1512–1521 (2024).
- ¹¹Agúndez, M., Cabezas, C., Tercero, B., Marcelino, N., Gallego, J. D., de Vicente, P., and Cernicharo, J., "Discovery of the propargyl radical (CH₂CCH) in TMC-1: One of the most abundant radicals ever found and a key species for cyclization to benzene in cold dark clouds," *Astron. Astrophys.* **647**, L10 (2021).
- ¹²Agúndez, M., Marcelino, N., Cabezas, C., Fuentetaja, R., Tercero, B., de Vicente, P., and Cernicharo, J., "Detection of the propargyl radical at λ 3 mm," *Astron. Astrophys.* **657**, A96 (2022).
- ¹³W. G. D. P. Silva, J. Cernicharo, S. Schlemmer, N. Marcelino, J.-C. Loison, M. Agúndez, D. Gupta, V. Wakelam, S. Thorwirth, C. Cabezas, B. Tercero, J. L. Doménech, R. Fuentetaja, W.-J. Kim, P. de Vicente, and O. Asvany, "Discovery of H₂CCCH⁺ in TMC-1," *Astron. Astrophys.* **676**, L1 (2023).
- ¹⁴K. Tanaka, Y. Sumiyoshi, Y. Ohshima, Y. Endo, and K. Kawaguchi, "Pulsed discharge nozzle Fourier transform microwave spectroscopy of the propargyl radical (H₂CCCH)," *J. Chem. Phys.* **107**, 2728–2733 (1997).
- ¹⁵E. Hebrard, M. Dobrijevic, J. C. Loison, A. Bergeat, K. M. Hickson, and F. Caralp, "Photochemistry of C₃H_p hydrocarbons in Titan's stratosphere revisited," *Astron. Astrophys.* **552**, A132 (2013).
- ¹⁶E. Herbst and C. M. Leung, "Gas-phase production of complex hydrocarbons, cyanopolynes, and related compounds in dense interstellar clouds," *Astrophys. J. Suppl. Ser.* **69**, 271–300 (1989).
- ¹⁷M. E. Jacox and D. E. Milligan, "Matrix isolation study of the vacuum ultraviolet photolysis of allene and methylacetylene. vibrational and electronic spectra of the species C₃, C₃H, C₃H₂, and C₃H₃," *Chem. Phys.* **4**, 45–61 (1974).
- ¹⁸E. B. Jochnowitz, X. Zhang, M. R. Nimlos, M. E. Varner, J. F. Stanton, and G. B. Ellison, "Propargyl radical: ab initio anharmonic modes and the polarized infrared absorption spectra of matrix-isolated HCCCH₂," *J. Phys. Chem. A* **109**, 3812–21 (2005).
- ¹⁹D. A. Ramsay and P. Thistlethwaite, "The electronic absorption spectrum of the propargyl radical," *Can. J. Phys.* **44**, 1381–1386 (1966).
- ²⁰A. Fahr and A. H. Laufer, "UV-absorption spectra of the radical transients generated from the 193-nm photolysis of allene, propyne, and 2-butyne," *J. Phys. Chem. A* **109**, 2534–9 (2005).
- ²¹P. Hemberger, M. Lang, B. Noller, I. Fischer, C. Alcaraz, B. K. Cunha de Miranda, G. A. Garcia, and H. Soldi-Lose, "Photoionization of Propargyl and Bromopropargyl Radicals: A Threshold Photoelectron Spectroscopic Study," *J. Phys. Chem. A* **115**, 2225–2230 (2011).
- ²²U. Jacovella, B. Gans, and F. Merkt, "On the adiabatic ionization energy of the propargyl radical," *J. Chem. Phys.* **139**, 084308 (2013).
- ²³G. A. Garcia, B. Gans, J. Krüger, F. Holzmeier, A. Röder, A. Lopes, C. Fittschen, C. Alcaraz, and J.-C. Loison, "Valence shell threshold photoelectron spectroscopy of C₃H_x (x = 0–3)," *Phys. Chem. Chem. Phys.* **20**, 8707–8718 (2018).
- ²⁴J. D. Savee, B. Sztáray, P. Hemberger, J. Zádor, A. Bodi, and D. L. Osborn, "Unimolecular isomerisation of 1,5-hexadiyne observed by threshold photoelectron photoion coincidence spectroscopy," *Faraday Discuss.* **238**, 645–664 (2022).
- ²⁵H.-J. Deyerl, I. Fischer, and P. Chen, "Photodissociation dynamics of the propargyl radical," *J. Chem. Phys.* **111**, 3441–3448 (1999).
- ²⁶X. Zheng, Y. Song, and J. Zhang, "Ultraviolet photodissociation dynamics of the propargyl radical," *J. Phys. Chem. A* **113**, 4604–12 (2009).
- ²⁷B. M. Broderick, N. Suas-David, N. Dias, and A. G. Suits, "Isomer-specific detection in the uv photodissociation of the propargyl radical by chirped-pulse mm-wave spectroscopy in a pulsed quasi-uniform flow," *Phys. Chem. Chem. Phys.* **20**, 5517–5529 (2018).
- ²⁸I. Savić and D. Gerlich, "Temperature variable ion trap studies of C₃H_n⁺ with H₂ and HD," *Phys. Chem. Chem. Phys.* **7**, 1026–1035 (2005).
- ²⁹I. Savić, S. Schlemmer, and D. Gerlich, "Low-Temperature Experiments on the Formation of Deuterated C₃H₃⁺," *ApJ* **621**, 1163 (2005).
- ³⁰L. Zhao, W. Lu, M. Ahmed, M. V. Zagidullin, V. N. Azyazov, A. N. Morozov, A. M. Mebel, and R. I. Kaiser, "Gas-phase synthesis of benzene via the propargyl radical self-reaction," *Sci. Adv.* **7**, eabf0360 (2021).
- ³¹H. R. Hrodmarsson, G. A. Garcia, L. Bourehil, L. Nahon, B. Gans, S. Boyé-Péronne, J.-C. Guillemin, and J.-C. Loison, "The isomer distribution of C₆H₆ products from the propargyl radical gas-phase recombination investigated by threshold-photoelectron spectroscopy," *Commun. Chem.* **7**, 156 (2024).
- ³²P. Constantinidis, F. Hirsch, I. Fischer, A. Dey, and A. M. Rijs, "Products of the Propargyl Self-Reaction at High Temperatures Investigated by IR/UV Ion Dip Spectroscopy," *J. Phys. Chem. A* **121**, 181–191 (2017).
- ³³J. A. Miller and S. J. Klippenstein, "The Recombination of Propargyl Radicals and Other Reactions on a C₆H₆ Potential," *J. Phys. Chem. A* **107**, 7783–7799 (2003).
- ³⁴J. D. Savee, T. M. Selby, O. Welz, C. A. Taatjes, and D. L. Osborn, "Time- and isomer-resolved measurements of sequential addition of acetylene to the propargyl radical," *J. Phys. Chem. Lett.* **6**, 4153–8 (2015).
- ³⁵T. M. Selby, F. Goulay, S. Soorkia, A. Ray, A. W. Jasper, S. J. Klippenstein, A. N. Morozov, A. M. Mebel, J. D. Savee, C. A. Taatjes, and D. L. Osborn, "Radical-Radical Reactions in Molecular Weight Growth: The Phenyl + Propargyl Reaction," *J. Phys. Chem. A* **127**, 2577–2590 (2023).
- ³⁶Z. Yang, G. R. Galimova, C. He, S. J. Goettl, D. Paul, W. Lu, M. Ahmed, A. M. Mebel, X. Li, and R. I. Kaiser, "Gas-phase formation of the resonantly stabilized 1-indenyl (C₉H₇⁺) radical in the interstellar medium," *Sci. Adv.* **9**, eadi5060 (2023).
- ³⁷J. Zhang, J. Gao, H. Wang, J. Guan, G. Xu, L. Xing, D. G. Truhlar, and Z. Wang, "Less-dominant resonance configuration of propargyl radical leads to a growth mechanism for polycyclic aromatic hydrocarbons that preserves the cyclopenta ring," *J. Am. Chem. Soc.* **147**, 9283–9293 (2025).
- ³⁸P. Lindstedt, L. Maurice, and M. Meyer, "Thermodynamic and kinetic issues in the formation and oxidation of aromatic species," *Faraday Discuss.* **119**, 409–432 (2002).
- ³⁹A. Matsugi and A. Miyoshi, "Computational study on the recombination reaction between benzyl and propargyl radicals," *Int. J. Chem. Kinet.* **44**, 206–218 (2012).
- ⁴⁰A. N. Morozov and A. M. Mebel, "Theoretical study of the reaction mechanism and kinetics of the phenyl + propargyl association," *Phys. Chem. Chem. Phys.* **22**, 6868–6880 (2020).
- ⁴¹R. Arns, R. McClish, P. Hemberger, A. Bodi, J. Bouwman, T. Kasper, and D. Schleier, "Is Phenylnitrene a Missing Link in the Formation of Polycyclic Aromatic Nitrogen Heterocycles?" *Angew. Chem. Int. Ed.* **64**, e202503940 (2025).
- ⁴²P. Stäuber, S. Doty, E. Van Dishoeck, and A. Benz, "X-ray chemistry in the envelopes around young stellar objects," *Astron. As-*

- trophys. **440**, 949–966 (2005).
- ⁴³M. Alagia, E. Bodo, P. Decleva, S. Falcinelli, A. Ponzi, R. Richter, and S. Stranges, “The soft X-ray absorption spectrum of the allyl free radical,” *Phys. Chem. Chem. Phys.* **15**, 1310–1318 (2013).
- ⁴⁴M. Alagia, M. Lavollée, R. Richter, U. Ekström, V. Carravetta, D. Stranges, B. Brunetti, and S. Stranges, “Probing the potential energy surface by high-resolution x-ray absorption spectroscopy: The umbrella motion of the core-excited CH₃ free radical,” *Phys. Rev. A* **76**, 022509 (2007).
- ⁴⁵U. Ekström, V. Carravetta, M. Alagia, M. Lavollée, R. Richter, C. Bolcato, and S. Stranges, “The umbrella motion of core-excited CH₃ and CD₃ methyl radicals,” *J. Chem. Phys.* **128**, 044302 (2008).
- ⁴⁶D. Schaffner, T. Juncker von Buchwald, E. Karaev, M. Alagia, R. Richter, S. Stranges, S. Coriani, and I. Fischer, “The x-ray absorption spectrum of the tert-butyl radical: An experimental and computational investigation,” *J. Chem. Phys.* **161**, 034309 (2024).
- ⁴⁷S. Reinwardt, P. Cieslik, T. Buhr, A. Perry-Sassmannshausen, S. Schippers, A. Müller, F. Trinter, and M. Martins, “Isomer-specific photofragmentation of C₃H₃⁺ at the carbon K-edge,” *Phys. Chem. Chem. Phys.* **26**, 15519–15529 (2024).
- ⁴⁸R. R. Blyth, R. Delaunay, M. Zitnik, J. Krempasky, R. Krempaska, J. Slezak, K. C. Prince, R. Richter, M. Vondracek, R. Camilloni, L. Avaldi, M. Coreno, G. Stefani, C. Furlani, M. de Simone, S. Stranges, and M. Y. Adam, “The high resolution Gas Phase Photoemission beamline, Elettra,” *J. Electron Spectrosc. Relat. Phenom.* **101-103**, 959–964 (1999).
- ⁴⁹M. Alagia, L. Avaldi, M. Coreno, R. Camilloni, C. Furlani, K. C. Prince, R. Richter, M. de Simone, G. Stefani, and S. Stranges, “The gas phase photoemission beamline at Elettra,” *Synchrotron Radiat. News* **16**, 19–27 (2003).
- ⁵⁰M. de Simone, M. Coreno, M. Alagia, R. Richter, and K. C. Prince, “Inner shell excitation spectroscopy of the tetrahedral molecules CX₄ (X = H, F, Cl),” *J. Phys. B: At. Mol. Opt. Phys.* **35**, 61 (2002).
- ⁵¹M. L. Vidal, X. Feng, E. Epifanovsky, A. I. Krylov, and S. Coriani, “A New and Efficient Equation-of-Motion Coupled-Cluster Framework for Core-Excited and Core-Ionized States,” *J. Chem. Theory Comput.* **15**, 3117–3133 (2019).
- ⁵²A. Dreuw and M. Wormit, “The algebraic diagrammatic construction scheme for the polarization propagator for the calculation of excited states,” *WIREs Comput. Mol. Sci.* **5**, 82–95 (2015).
- ⁵³E. Epifanovsky, A. T. B. Gilbert, X. Feng, J. Lee, Y. Mao, N. Mardirossian, P. Pokhilko, A. F. White, M. P. Coons, A. L. Dempwolf, Z. Gan, D. Hait, P. R. Horn, L. D. Jacobson, I. Kaliman, J. Kussmann, A. W. Lange, K. U. Lao, D. S. Levine, J. Liu, S. C. McKenzie, A. F. Morrison, K. D. Nanda, F. Plasser, D. R. Rehn, M. L. Vidal, Z.-Q. You, Y. Zhu, B. Alam, B. J. Albrecht, A. Aldossary, E. Alguire, J. H. Andersen, V. Athavale, D. Barton, K. Begam, A. Behn, N. Bellonzi, Y. A. Bernard, E. J. Berquist, H. G. A. Burton, A. Carreras, K. Carter-Fenk, R. Chakraborty, A. D. Chien, K. D. Closser, V. Cofer-Shabica, S. Dasgupta, M. de Wergifosse, J. Deng, M. Diedenhofen, H. Do, S. Ehlert, P.-T. Fang, S. Fatehi, Q. Feng, T. Friedhoff, J. Gayvert, Q. Ge, G. Gidofalvi, M. Goldey, J. Gomes, C. E. González-Espinoza, S. Gulania, A. O. Gunina, M. W. D. Hanson-Heine, P. H. P. Harbach, A. Hauser, M. F. Herbst, M. Hernández Vera, M. Hodecker, Z. C. Holden, S. Houck, X. Huang, K. Hui, B. C. Huynh, M. Ivanov, A. Jász, H. Ji, H. Jiang, B. Kaduk, S. Kähler, K. Khistyayev, J. Kim, G. Kis, P. Klunzinger, Z. Koczor-Benda, J. H. Koh, D. Kosenkov, L. Koullias, T. Kowalczyk, C. M. Krauter, K. Kue, A. Kunitsa, T. Kus, I. Ladjánszki, A. Landau, K. V. Lawler, D. Lefrancois, S. Lehtola, R. R. Li, Y.-P. Li, J. Liang, M. Liebenthal, H.-H. Lin, Y.-S. Lin, F. Liu, K.-Y. Liu, M. Loipersberger, A. Luenser, A. Manjanath, P. Manohar, E. Mansoor, S. F. Manzer, S.-P. Mao, A. V. Marenich, T. Markovich, S. Mason, S. A. Maurer, P. F. McLaughlin, M. F. S. J. Menger, J.-M. Mewes, S. A. Mewes, P. Morgante, J. W. Mullinax, K. J. Oosterbaan, G. Paran, A. C. Paul, S. K. Paul, F. Pavošević, Z. Pei, S. Prager, E. I. Proynov, Á. Rák, E. Ramos-Cordoba, B. Rana, A. E. Rask, A. Rettig, R. M. Richard, F. Rob, E. Rossomme, T. Scheele, M. Scheurer, M. Schneider, N. Sergueev, S. M. Sharada, W. Skomorowski, D. W. Small, C. J. Stein, Y.-C. Su, E. J. Sundstrom, Z. Tao, J. Thirman, G. J. Tornai, T. Tsuchimochi, N. M. Tubman, S. P. Veccham, O. Vydrov, J. Wenzel, J. Witte, A. Yamada, K. Yao, S. Yeganeh, S. R. Yost, A. Zech, I. Y. Zhang, X. Zhang, Y. Zhang, D. Zuev, A. Aspuru-Guzik, A. T. Bell, N. A. Besley, K. B. Bravaya, B. R. Brooks, D. Casanova, J.-D. Chai, S. Coriani, C. J. Cramer, G. Cserey, A. E. DePrince, R. A. DiStasio, A. Dreuw, B. D. Dunietz, T. R. Furlani, W. A. Goddard, S. Hammes-Schiffer, T. Head-Gordon, W. J. Hehre, C.-P. Hsu, T.-C. Jagau, Y. Jung, A. Klamt, J. Kong, D. S. Lambrecht, W. Liang, N. J. Mayhall, C. W. McCurdy, J. B. Neaton, C. Ochsenfeld, J. A. Parkhill, R. Peverati, V. A. Rassolov, Y. Shao, L. V. Slipchenko, T. Stauch, R. P. Steele, J. E. Subotnik, A. J. W. Thom, A. Tkatchenko, D. G. Truhlar, T. Van Voorhis, T. A. Wesolowski, K. B. Whaley, H. L. Woodcock, P. M. Zimmerman, S. Faraji, P. M. W. Gill, M. Head-Gordon, J. M. Herbert, and A. I. Krylov, “Software for the frontiers of quantum chemistry: An overview of developments in the Q-Chem 5 package,” *J. Chem. Phys.* **155**, 084801 (2021).
- ⁵⁴T. Clark, J. Chandrasekhar, G. W. Spitznagel, and P. V. R. Schleyer, “Efficient diffuse function-augmented basis sets for anion calculations. III. The 3-21+G basis set for first-row elements, Li-F,” *J. Comput. Chem.* **4**, 294–301 (1983).
- ⁵⁵R. Krishnan, J. S. Binkley, R. Seeger, and J. A. Pople, “Self-consistent molecular orbital methods. XX. A basis set for correlated wave functions,” *J. Chem. Phys.* **72**, 650–654 (1980).
- ⁵⁶O. Marchetti and H.-J. Werner, “Accurate calculations of intermolecular interaction energies using explicitly correlated wave functions,” *Phys. Chem. Chem. Phys.* **10**, 3400–3409 (2008).
- ⁵⁷T. H. Dunning, “Gaussian basis sets for use in correlated molecular calculations. I. The atoms boron through neon and hydrogen,” *J. Chem. Phys.* **90**, 1007–1023 (1989).
- ⁵⁸R. A. Kendall, T. H. Dunning, and R. J. Harrison, “Electron affinities of the first-row atoms revisited. systematic basis sets and wave functions,” *J. Chem. Phys.* **96**, 6796–6806 (1992).
- ⁵⁹T. B. Adler, G. Knizia, and H.-J. Werner, “A simple and efficient coupled CCSD(T)-F12 approximation,” *J. Chem. Phys.* **127**, 221106 (2007).
- ⁶⁰G. Knizia, T. B. Adler, and H.-J. Werner, “Simplified CCSD(T)-F12 methods: Theory and benchmarks,” *J. Chem. Phys.* **130**, 054104 (2009).
- ⁶¹K. A. Peterson, T. B. Adler, and H.-J. Werner, “Systematically convergent basis sets for explicitly correlated wavefunctions: The atoms H, He, B-Ne, and Al-Ar,” *J. Chem. Phys.* **128**, 084102 (2008).
- ⁶²A. I. Krylov, “From orbitals to observables and back,” *J. Chem. Phys.* **153**, 080901 (2020).
- ⁶³DTU Computing Center, “DTU Computing Center resources,” (2024), <https://doi.org/10.48714/DTU.HPC.0001>.
- ⁶⁴R. Crespo-Otero and M. Barbatti, “Spectrum simulation and decomposition with nuclear ensemble: formal derivation and application to benzene, furan and 2-phenylfuran,” *Theor. Chem. Acc.* **131**, 1237 (2012).
- ⁶⁵P. J. Stephens, F. J. Devlin, C. F. Chabalowski, and M. J. Frisch, “Ab initio calculation of vibrational absorption and circular dichroism spectra using density functional force fields,” *J. Phys. Chem.* **98**, 11623–11627 (1994).
- ⁶⁶F. J. Avila Ferrer and F. Santoro, “Comparison of vertical and adiabatic harmonic approaches for the calculation of the vibrational structure of electronic spectra,” *Phys. Chem. Chem. Phys.* **14**, 13549–13563 (2012).
- ⁶⁷J. Cerezo and F. Santoro, “*FCclasses3*: Vibrationally-resolved spectra simulated at the edge of the harmonic approximation,” *J. Comput. Chem.* **44**, 626–643 (2023).

- ⁶⁸P. Macak, Y. Luo, and H. Ågren, "Simulations of vibronic profiles in two-photon absorption," *Chem. Phys. Lett.* **330**, 447–456 (2000).
- ⁶⁹M. Biczysko, J. Bloino, F. Santoro, and V. Barone, "Time-independent approaches to simulate electronic spectra line-shapes: From small molecules to macrosystems," in *Computational strategies for spectroscopy* (Wiley Online Library, 2012) pp. 361–443.
- ⁷⁰M. Frisch, G. W. Trucks, H. B. Schlegel, G. E. Scuseria, M. Robb, J. R. Cheeseman, G. Scalmani, V. Barone, G. A. Petersson, H. Nakatsuji, *et al.*, "Gaussian 16," (2016).
- ⁷¹Q. Sun, T. C. Berkelbach, N. S. Blunt, G. H. Booth, S. Guo, Z. Li, J. Liu, J. D. McClain, E. R. Sayfutyarova, S. Sharma, S. Wouters, and G. K.-L. Chan, "PySCF: the Python-based simulations of chemistry framework," *WIREs Comput. Mol. Sci.* **8**, e1340 (2018).
- ⁷²Q. Sun, X. Zhang, S. Banerjee, P. Bao, M. Barbry, N. S. Blunt, N. A. Bogdanov, G. H. Booth, J. Chen, Z.-H. Cui, J. J. Eriksen, Y. Gao, S. Guo, J. Hermann, M. R. Hermes, K. Koh, P. Koval, S. Lehtola, Z. Li, J. Liu, N. Mardirossian, J. D. McClain, M. Motta, B. Mussard, H. Q. Pham, A. Pulkin, W. Purwanto, P. J. Robinson, E. Ronca, E. R. Sayfutyarova, M. Scheurer, H. F. Schurkus, J. E. T. Smith, C. Sun, S.-N. Sun, S. Upadhyay, L. K. Wagner, X. Wang, A. White, J. D. Whitfield, M. J. Williamson, S. Wouters, J. Yang, J. M. Yu, T. Zhu, T. C. Berkelbach, S. Sharma, A. Y. Sokolov, and G. K.-L. Chan, "Recent developments in the PySCF program package," *J. Chem. Phys.* **153**, 024109 (2020).
- ⁷³M. F. Herbst, M. Scheurer, T. Fransson, D. R. Rehn, and A. Dreuw, "adcc: A versatile toolkit for rapid development of algebraic-diagrammatic construction methods," *WIREs Comput. Mol. Sci.* **10**, e1462 (2020).
- ⁷⁴I. E. Brumboiu, "cvs-adc-grad," <https://gitlab.com/iubrcvs-adc-grad> (2025).
- ⁷⁵L.-P. Wang and C. Song, "Geometry optimization made simple with translation and rotation coordinates," *J. Chem. Phys.* **144**, 214108 (2016).
- ⁷⁶J. L. Holmes and F. P. Lossing, "The reactivity of $[C_3H_3^+]$ ions; a thermochemical study," *Can. J. Chem.* **57**, 249–252 (1979).
- ⁷⁷T. Schüßler, W. Roth, T. Gerber, C. Alcaraz, and I. Fischer, "The VUV photochemistry of radicals: C_3H_3 and C_2H_5 ," *Phys. Chem. Chem. Phys.* **7**, 819–825 (2005).

Supplementary Information.**The X-ray absorption spectrum of the propargyl radical, $C_3H_3\cdot$.**

Dorothee Schaffner,¹ Theo Juncker von Buchwald,² Jacob Pedersen,^{2, 3} Andreas Rasp,¹ Emil Karaev,¹ Valentin von Laffert,¹ Alessio Bruno,⁴ Michele Alagia,⁵ Stefano Stranges,^{5, 4} Ingo Fischer,^{1, a)} and Sonia Coriani^{2, b)}

¹⁾*Institute of Physical and Theoretical Chemistry, University of Würzburg, D-97074 Würzburg, Germany.*

²⁾*DTU Chemistry, Technical University of Denmark, DK-2800 Kgs. Lyngby, Denmark.*

³⁾*Department of Chemistry, Norwegian University of Science and Technology, N-7491 Trondheim, Norway.*

⁴⁾*Dipartimento di Chimica e Tecnologia dei Farmaci, Università degli Studi di Roma "La Sapienza", piazzale Aldo Moro 5, I-00185 Rome, Italy.*

⁵⁾*CNR - Istituto Officina dei Materiali (IOM), Laboratorio TASC, 34149 Trieste, Italy.*

(Dated: 24 February 2026)

^{a)}E-mail: ingo.fischer@uni-wuerzburg.de (experiment)

^{b)}E-mail: soco@kemi.dtu.dk (theory)

CONTENT

This SI contains:

S1. TOF mass spectra at different excitation energies

S2. Computational information

S2.1 Extended Computational Details

S2.2 X-ray absorption spectra from fc-CVS-EOM-CCSD and CVS-ADC(2)-x

S2.3 Core Ionization Energies

S2.4 Excitation Energies and Oscillator Strengths

S2.5 Natural Transition Orbitals (NTOs)

S2.6 Vibrationally Resolved Spectra

S2.7 Optimized structures

S2.8 FCclasses3 input file example

S1. TOF MASS SPECTRA AT DIFFERENT EXCITATION ENERGIES

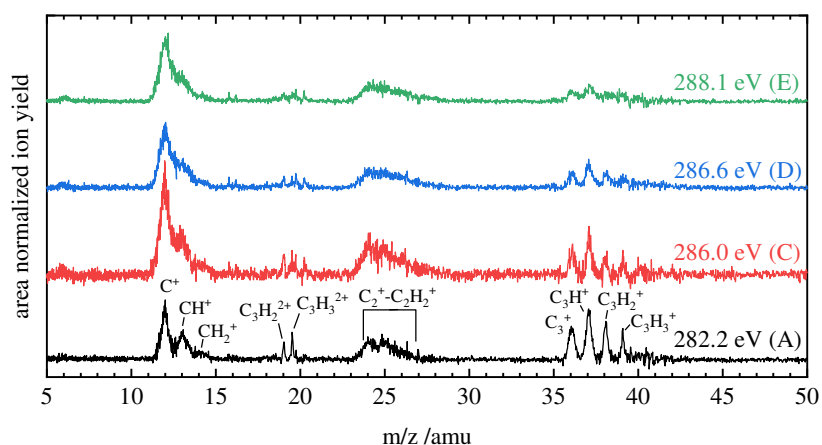


FIG. S1. TOF mass spectra of single ion events upon excitation of the propargyl radical at a photon energy of 282.2 eV (band A), 286.0 eV (band C), 286.6 eV (band D) and 288.1 eV (band E).

Fig. S1 shows a comparison of the single ion mass spectra after excitation at 282.2 eV (band A), 286.0 eV (band C), 286.6 eV (band D) and 288.1 eV (band E). The spectra were obtained after subtraction of the contribution from off-resonant ionization which was recorded at 280.2 eV.

The precursor shows resonant absorptions in the regions of 286.0 eV (band C), 286.6 eV (band D) and 288.1 eV (band E). To obtain a spectrum of purely the propargyl radical for these excitation energies, the spectrum of the precursor was measured at the same photon energy at 0 W and (after its correction for off-resonant contributions) subtracted. This additional correction procedure results in a lower signal to noise ratio, especially at 286.0 eV (band C). All four spectra show the formation of the same fragment ions, whose branching ratios are summarized in Table S1. Small, sharp signals observed at m/z 40.5/39.5 (Br^{2+}), 27/26.34 (Br^{3+}), 20.25/19.75 (Br^{4+}), 16.2/15.8 (Br^{5+}) result from the bromine radical that is not completely subtracted by the correction for the off-resonant contribution. For higher excitations the relative intensity of the C_3 fragments decreases significantly from more than 30% to below 20%, whereas the branching ratios for C_2 and C_1 fragments increase correspondingly. In addition, the ratio between the fragments C_1 and C_2 increases with the excitation energy. This shows that the fragmentation tendency increases with the excitation of higher core excited states as was observed for the *tert*-butyl radical.¹

TABLE S1. Branching ratios of single ion events after excitation of the propargyl radical at different resonances. Relative intensities were determined from the mass spectrum (Fig. S1) by integration. Integrals of overlapping masses were derived from fitting with Gauss functions. The branching ratios were normalized so that all channels sum up to 100%. Very low branching ratios are not specified and are summarized in “others”. The error of each branching ratio is estimated to be around $\pm 20\%$ of the respective branching ratio.

m/z	species	282.2 eV /%	286.0 eV /%	286.6 eV /%	288.1 eV /%
39	$C_3H_3^+$	4	2	2	2
38	$C_3H_2^+$	8	2	5	4
37	C_3H^+	13	6	8	7
36	C_3^+	10	4	5	4
26	$C_2H_2^+$	6	8	9	7
25	C_2H^+	12	9	8	7
24	C_2^+	9	13	11	11
19.5	$C_3H_3^{2+}$	2	–	–	–
19	$C_3H_2^{2+}$	–	–	–	–
14	CH_2^+	4	3	3	4
13	CH^+	13	18	17	15
12	C^+	17	30	29	35
6	C^{2+}	–	–	–	2
others		2	2	3	3

S2. COMPUTATIONAL INFORMATION

S2.1. Extended Computational Details

The X-ray absorption spectrum of the propargyl radical is calculated using the frozen-core core-valence-separated equation-of-motion coupled cluster singles and doubles (fc-CVS-EOM-CCSD) method² in Q-Chem 6.2³ using both restricted open-shell (ROHF) and unrestricted (UHF) Hartree-Fock reference orbitals. We used the optimized ground state structure by Botschwina and Oswald⁴ obtained at the CCSD(T*)-F12a^{5,6}/cc-pVTZ-F12⁷ level of theory. The X-ray absorption spectrum is calculated using the 6-311++G** basis set,⁸⁻¹⁰ the cc-pVTZ basis set,¹¹ and the aug-cc-pVTZ basis set.¹² When reporting the results, we use usual C_{2v} point group symmetry conventions, i.e. the molecule is oriented such that the C_2 rotational axis is aligned with the Z-axis and the molecular plane in the YZ-plane. We calculated 15 excitations in each irreducible representation (irrep). The ground state belongs to the B_1 irrep. The spectra were found to be of comparable quality regardless of the reference orbitals and basis sets. To test the fc-CVS-EOM-CCSD results we also calculate the X-ray absorption spectrum at the CVS-ADC(2)-x level using UHF reference orbitals and the aug-cc-pVTZ basis set in Q-Chem 6.2. For the assignment of spectral peaks we calculated natural transition orbitals (NTOs)^{2,13} of both fc-CVS-EOM-CCSD and CVS-ADC(2)-x using the aug-cc-pVTZ basis set.

To investigate the vibrational effects in the X-ray absorption spectra we adopted (i) the nuclear ensemble approach (NEA) and (ii) *a posteriori* treatment based on Franck-Condon (FC) factors and time-dependent spectra computed within the harmonic approximation with FCclasses3.¹⁴ In the NEA the vibrational effects are captured by computing the X-ray absorption spectrum at numerous vibrationally distorted geometries. We sampled 200 structures from a Wigner distribution at a temperature of 300 K. The FC vibrational treatment requires optimized core-excited state structures, and we used the Vertical Gradient (VG) and Adiabatic Shift (AS) methods.^{15,16} We note that the VG approach requires the ground state gradient and Hessian as well as the transition dipole strength. We optimized the first three bright transitions (the first, second, and fifth electronic excitations) at the CVS-ADC(2)-x/aug-cc-pVDZ level of theory in cvs-adc-grad¹⁷ in conjunction with ADCC¹⁸ and PySCF.^{19,20} The electronic transition dipole strengths used in both vibrational treatments were obtained at the fc-CVS-EOM-CCSD/aug-cc-pVTZ and CVS-ADC(2)-x/aug-cc-pVTZ levels of theory using Q-Chem 6.2.

All calculations were carried out on the DTU HPC resources.²¹

S2.2. X-ray absorption spectra from fc-CVS-EOM-CCSD and CVS-ADC(2)-x

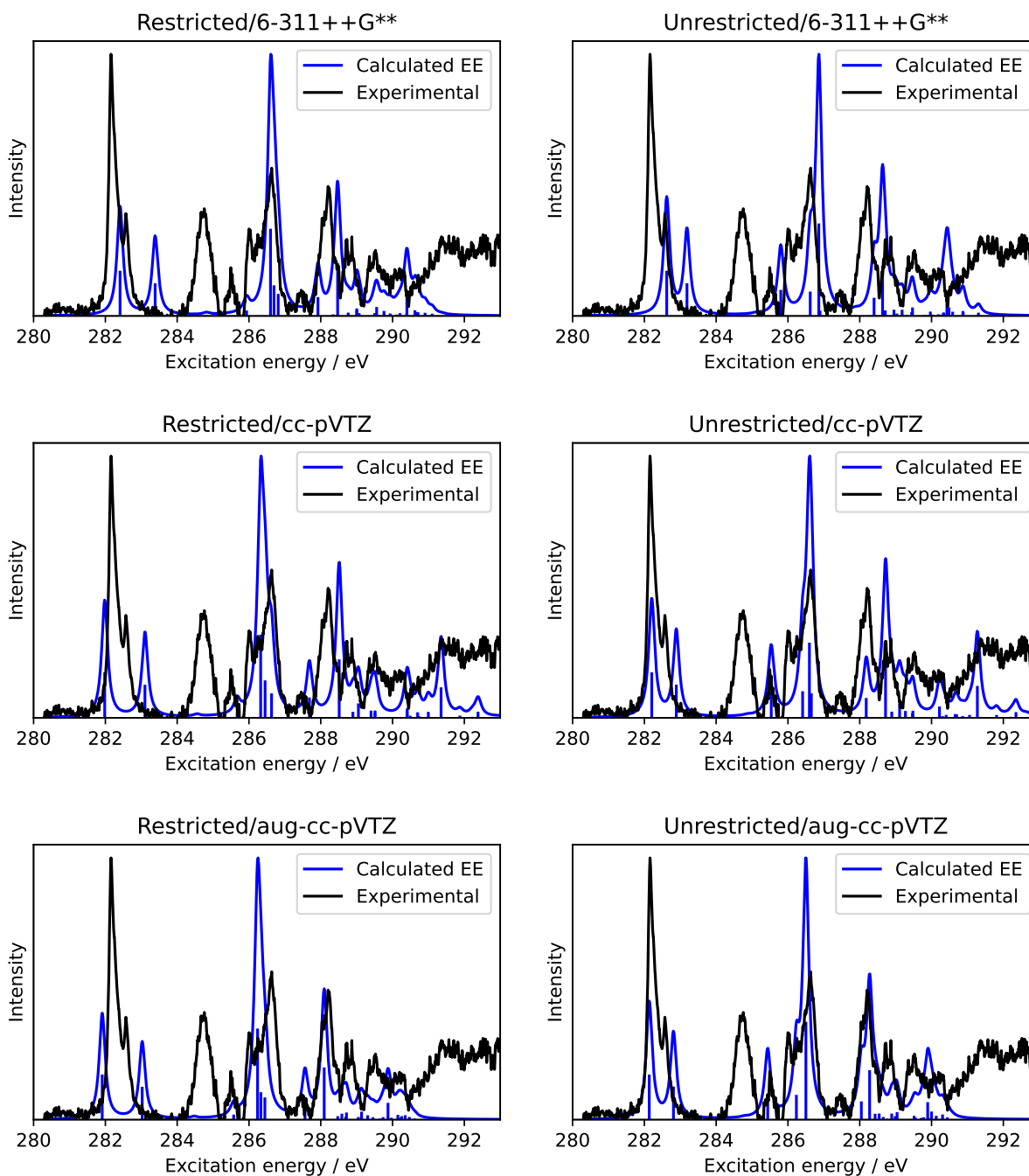


FIG. S2. Comparison between the experimental spectrum (black line) and the simulated fc-CVS-EOM-CCSD X-ray absorption spectra of the propargyl radical with (top left) ROHF/6-311++G**, (top right) UHF/6-311++G**, (middle left) ROHF/cc-pVTZ, (middle right) UHF/cc-pVTZ, (bottom left) ROHF/aug-cc-pVTZ, and (bottom right) UHF/aug-cc-pVTZ levels of theory in blue. The sticks were convoluted using a Lorentzian lineshape with a full width at half maximum (FWHM) of 200 meV.

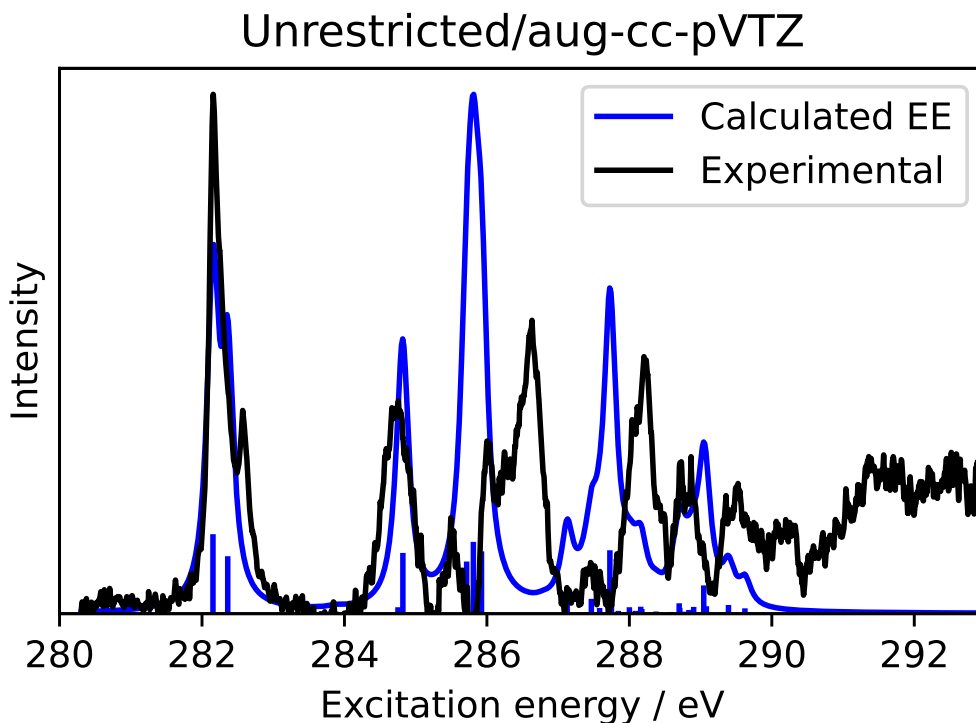


FIG. S3. Comparison between the experimental spectrum (black line) and the simulated CVS-ADC(2)-x/aug-cc-pVTZ X-ray absorption spectra (blue line) of the propargyl radical. The sticks were convoluted using a Lorentzian lineshape with a FWHM of 200 meV.

S2.3. Core Ionization Energies

TABLE S2. C1s core ionization energies (in eV) of the propargyl radical computed at the fc-CVS-EOM-IP-CCSD/aug-cc-pVTZ level of theory. The respective carbon atom is highlighted in the last column. The multiplicity stated in the table refers to the cationic final state reached by the ionization. For the $2 B_1$ ionized state $[(2a_1)^{-1}]$, we note that the triplet has a higher ionization energy than the singlet.

IP state	Ionisation	ROHF		UHF		Carbon
		singlet	triplet	singlet	triplet	
$1 B_1$	$(3a_1)^{-1}$	291.4878	291.2337	291.4734	291.1673	H ₂ CC <u>C</u> H
$2 B_1$	$(2a_1)^{-1}$	291.6181	291.7696	291.7233	291.8698	H ₂ CC <u>C</u> H
$3 B_1$	$(1a_1)^{-1}$	292.6061	291.9766	292.5449	291.9304	H ₂ <u>C</u> CCH

S2.4. Excitation Energies and Oscillator Strengths

TABLE S3: fc-CVS-EOM-CCSD and CVS-ADC(2)-x results for the excitation energies (in eV) and oscillator strengths (f) of the propargyl radical, using either UHF or ROHF (only fc-CVS-EOM-CCSD) reference and the aug-cc-pVTZ basis sets. Transitions that are included in Tables S5 and S6 are shown in gray. The ground state is \tilde{X}^2B_1 .

Final state	fc-CVS-EOM-CCSD				CVS-ADC(2)-x	
	ROHF reference		UHF reference		UHF reference	
	Energy (eV)	f	Energy (eV)	f	Energy (eV)	f
1 2A_1	281.9118	0.0345	282.1359	0.0345	282.1539	0.0306
2 2A_1	283.0258	0.0251	282.8106	0.0253	282.3613	0.0221
3 2A_1	284.4676	0.0006	284.7728	0.0002	283.8704	0.0002
4 2A_1	286.4429	0.0170	286.2346	0.0189	285.7153	0.0201
5 2A_1	287.5605	0.0146	288.0442	0.0139	287.1269	0.0067
6 2A_1	288.0958	0.0399	288.2749	0.0378	287.4665	0.0057
7 2A_1	288.7771	0.0000	288.6950	0.0000	287.7263	0.0244
8 2A_1	289.4533	0.0019	289.5929	0.0004	288.6501	0.0000
9 2A_1	289.8061	0.0001	289.6945	0.0001	288.6995	0.0040
10 2A_1	289.8734	0.0128	289.7803	0.0018	288.8622	0.0000
11 2A_1	289.9228	0.0004	289.8926	0.0134	289.0442	0.0109
12 2A_1	290.1483	0.0036	289.9998	0.0062	289.0809	0.0029
13 2A_1	290.3517	0.0034	290.3069	0.0040	289.4635	0.0000
14 2A_1	290.4686	0.0020	290.5788	0.0000	289.4754	0.0001
15 2A_1	290.6090	0.0008	290.5813	0.0002	289.6362	0.0003
1 2A_2	285.4798	0.0001	285.3688	0.0003	284.7513	0.0025
2 2A_2	285.5746	0.0038	285.4364	0.0198	284.8203	0.0234
3 2A_2	286.2398	0.0696	286.4998	0.0748	285.8099	0.0277
4 2A_2	286.3313	0.0210	286.5326	0.0001	285.9240	0.0240
5 2A_2	288.5880	0.0045	288.5411	0.0047	287.7485	0.0034
6 2A_2	289.0470	0.0021	288.9873	0.0027	288.0003	0.0025

7 ² A ₂	289.1364	0.0061	289.0403	0.0057	288.1750	0.0018
8 ² A ₂	289.3071	0.0033	289.3753	0.0003	288.2939	0.0000
9 ² A ₂	289.5280	0.0002	289.5154	0.0029	288.7077	0.0022
10 ² A ₂	289.7009	0.0002	289.7118	0.0013	288.8349	0.0014
11 ² A ₂	289.7363	0.0019	289.8679	0.0004	288.9027	0.0026
12 ² A ₂	289.9674	0.0014	289.9122	0.0014	289.0198	0.0001
13 ² A ₂	290.2199	0.0014	290.1307	0.0029	289.1723	0.0000
14 ² A ₂	290.2539	0.0027	290.2902	0.0000	289.3913	0.0034
15 ² A ₂	290.4324	0.0003	290.4423	0.0018	289.6223	0.0021
1 ² B ₁	287.6665	0.0002	287.6212	0.0004	286.7873	0.0002
2 ² B ₁	287.9761	0.0004	287.8897	0.0004	287.1690	0.0000
3 ² B ₁	288.1053	0.0010	288.1946	0.0002	287.2745	0.0004
4 ² B ₁	288.3737	0.0002	288.2723	0.0002	287.3794	0.0006
5 ² B ₁	288.4731	0.0027	288.4283	0.0045	287.5827	0.0022
6 ² B ₁	288.6016	0.0000	288.6555	0.0020	287.8454	0.0011
7 ² B ₁	288.6979	0.0022	288.7501	0.0000	287.9145	0.0001
8 ² B ₁	288.7168	0.0055	288.8905	0.0046	288.0841	0.0011
9 ² B ₁	289.1461	0.0002	289.0523	0.0000	288.1594	0.0027
10 ² B ₁	289.3444	0.0004	289.4157	0.0004	288.3746	0.0008
11 ² B ₁	289.4759	0.0005	289.4661	0.0001	288.4109	0.0000
12 ² B ₁	289.6054	0.0004	289.5514	0.0015	288.5825	0.0007
13 ² B ₁	289.6514	0.0007	289.5692	0.0000	288.7603	0.0008
14 ² B ₁	289.7167	0.0003	289.9055	0.0003	289.0554	0.0002
15 ² B ₁	289.9379	0.0001	290.0618	0.0001	289.1824	0.0001

TABLE S4: fc-CVS-EOM-CCSD results for the excitation energies (in eV) and oscillator strengths (f) of the propargyl radical, using either UHF or ROHF reference and two different basis sets. Electronic states are sorted per irreducible representation. The ground state is \tilde{X}^2B_1 .

Final state	6-311++G**				cc-pVTZ			
	UHF reference		ROHF reference		UHF reference		ROHF reference	
	Energy (eV)	f	Energy (eV)	f	Energy (eV)	f	Energy (eV)	f
1 2A_1	282.4086	0.0345	282.6229	0.0345	282.2056	0.0347	281.9812	0.0347
2 2A_1	283.3861	0.0249	283.1869	0.0250	282.8897	0.0254	283.1022	0.0252
3 2A_1	284.8117	0.0006	285.1108	0.0003	284.8573	0.0003	284.5501	0.0006
4 2A_1	286.8146	0.0168	286.6201	0.0186	286.4086	0.0203	286.6293	0.0188
5 2A_1	287.9220	0.0144	288.3984	0.0139	288.1798	0.0151	287.6841	0.0155
6 2A_1	288.4702	0.0403	288.6357	0.0384	288.7187	0.0437	288.5134	0.0446
7 2A_1	289.1469	0.0001	289.0631	0.0000	289.4690	0.0036	289.5083	0.0040
8 2A_1	289.9334	0.0019	290.0664	0.0004	290.2215	0.0087	290.4089	0.0071
9 2A_1	290.3775	0.0000	290.2587	0.0000	291.0596	0.0022	290.9964	0.0046
10 2A_1	290.3999	0.0164	290.3331	0.0027	294.1167	0.0001	294.0840	0.0007
11 2A_1	290.4845	0.0001	290.4282	0.0159	294.5142	0.0013	294.5371	0.0017
12 2A_1	290.6223	0.0044	290.4862	0.0066	294.7643	0.0337	294.7324	0.0328
13 2A_1	290.9049	0.0025	290.8742	0.0038	295.0770	0.0041	295.2067	0.0025
14 2A_1	291.1043	0.0017	291.3012	0.0001	295.2898	0.0407	295.3303	0.0410
15 2A_1	291.3588	0.0002	291.3073	0.0025	295.8039	0.0049	295.6744	0.0055
1 2A_2	285.8427	0.0001	285.7346	0.0002	285.4664	0.0007	285.5833	0.0000
2 2A_2	285.9338	0.0042	285.8002	0.0199	285.5344	0.0201	285.6714	0.0042
3 2A_2	286.6000	0.0666	286.8594	0.0707	286.5977	0.0574	286.3260	0.0636
4 2A_2	286.6972	0.0234	286.8934	0.0040	286.6514	0.0187	286.4492	0.0286
5 2A_2	289.0048	0.0046	288.9527	0.0048	288.8919	0.0047	288.8958	0.0045
6 2A_2	289.5016	0.0021	289.4464	0.0029	289.2728	0.0052	289.4003	0.0055
7 2A_2	289.5570	0.0069	289.4699	0.0065	290.6580	0.0029	290.6990	0.0042
8 2A_2	289.7613	0.0038	289.8033	0.0002	291.2767	0.0244	291.3516	0.0233
9 2A_2	289.9594	0.0003	289.9671	0.0033	292.0554	0.0001	292.1860	0.0002

10 ² A ₂	290.1500	0.0000	290.1907	0.0013	292.2138	0.0008	292.2264	0.0007
11 ² A ₂	290.2074	0.0022	290.3088	0.0011	292.5841	0.0001	292.4240	0.0006
12 ² A ₂	290.3968	0.0021	290.3454	0.0019	292.6530	0.0007	292.4578	0.0000
13 ² A ₂	290.6573	0.0030	290.5882	0.0032	293.9671	0.0031	293.9882	0.0013
14 ² A ₂	290.7105	0.0028	290.7855	0.0003	294.5844	0.0220	294.5188	0.0249
15 ² A ₂	290.9425	0.0005	290.8826	0.0028	294.8267	0.0069	294.9005	0.0025
1 ² B ₁	287.9224	0.0002	287.8728	0.0005	288.2358	0.0007	288.2672	0.0002
2 ² B ₁	288.3442	0.0012	288.2767	0.0005	288.4986	0.0004	288.5707	0.0003
3 ² B ₁	288.3638	0.0004	288.4443	0.0004	289.1105	0.0107	289.0494	0.0110
4 ² B ₁	288.6269	0.0002	288.5248	0.0004	289.4800	0.0054	289.5130	0.0056
5 ² B ₁	288.7638	0.0025	288.7102	0.0042	289.7680	0.0001	289.8586	0.0001
6 ² B ₁	288.8680	0.0000	289.0172	0.0003	290.2500	0.0010	290.1775	0.0001
7 ² B ₁	289.0029	0.0058	289.0342	0.0018	290.3139	0.0012	290.3320	0.0000
8 ² B ₁	289.0697	0.0021	289.1799	0.0048	290.4071	0.0022	290.4035	0.0055
9 ² B ₁	289.3930	0.0002	289.3006	-0.0000	290.6992	0.0026	290.4894	0.0016
10 ² B ₁	289.6057	0.0005	289.7522	0.0002	290.8658	0.0013	290.7364	0.0012
11 ² B ₁	289.8530	0.0006	289.7904	0.0007	291.8116	0.0021	291.8761	0.0017
12 ² B ₁	289.9621	0.0004	289.8920	0.0005	291.8803	0.0000	291.9192	0.0000
13 ² B ₁	290.0814	0.0003	290.0213	0.0010	292.2258	0.0002	292.3016	0.0003
14 ² B ₁	290.1147	0.0011	290.2737	0.0004	292.3517	0.0044	292.3812	0.0047
15 ² B ₁	290.3320	0.0002	290.4565	0.0001	292.5758	0.0001	292.5004	0.0000

S2.5. Natural Transition Orbitals (NTOs)

TABLE S5. NTOs from (unrestricted) fc-CVS-EOM-CCSD/aug-cc-pVTZ calculations for selected core excitations (MO isovalue = 0.05). The ground state is \tilde{X}^2B_1 .

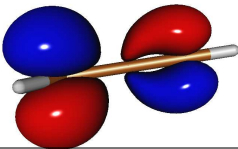
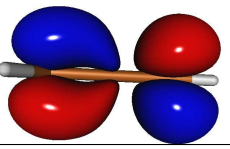
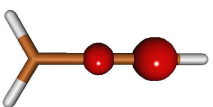
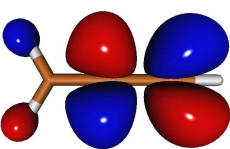
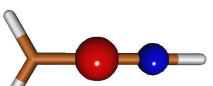
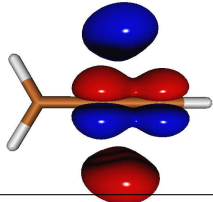
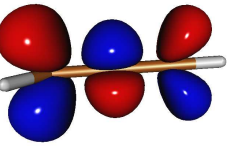
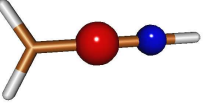
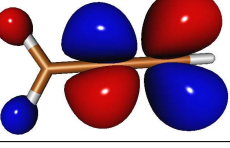
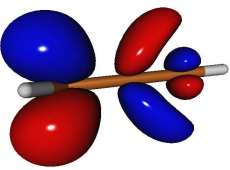
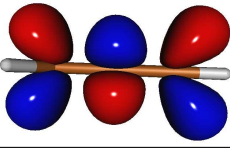
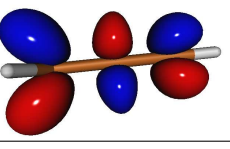
	Hole	Particle	Hole	Particle
A E = 282.136 eV f = 0.0345 1^2A_1				
A E = 282.811 eV f = 0.0253 2^2A_1				
B E = 285.436 eV f = 0.0198 2^2A_2				
C E = 286.235 eV f = 0.0189 4^2A_1				
D E = 286.500 eV f = 0.0747 3^2A_2				
E E = 288.044 eV f = 0.0139 5^2A_1				
E E = 288.275 eV f = 0.037774 6^2A_1				
E = 289.893 eV f = 0.0133 11^2A_1				

TABLE S6. NTOs from (unrestricted) CVS-ADC(2)-x/aug-cc-pVTZ for selected core excitations (MO isovalue = 0.05). The ground state is \tilde{X}^2B_1 .

	Hole	Particle	Hole	Particle
A E = 282.154 eV f = 0.0306 1^2A_1				
A E = 282.361 eV f = 0.0221 2^2A_1				
B E = 284.820 eV f = 0.0234 2^2A_2				
C-D E = 285.715 eV f = 0.0201 4^2A_1				
C-D E = 285.810 eV f = 0.0277 3^2A_2				
C-D E = 285.924 eV f = 0.024001 4^2A_2				
E E = 287.726 eV f = 0.0244 7^2A_1				
E = 289.044 eV f = 0.0109 11^2A_1				

S2.6. Vibrationally Resolved Spectra

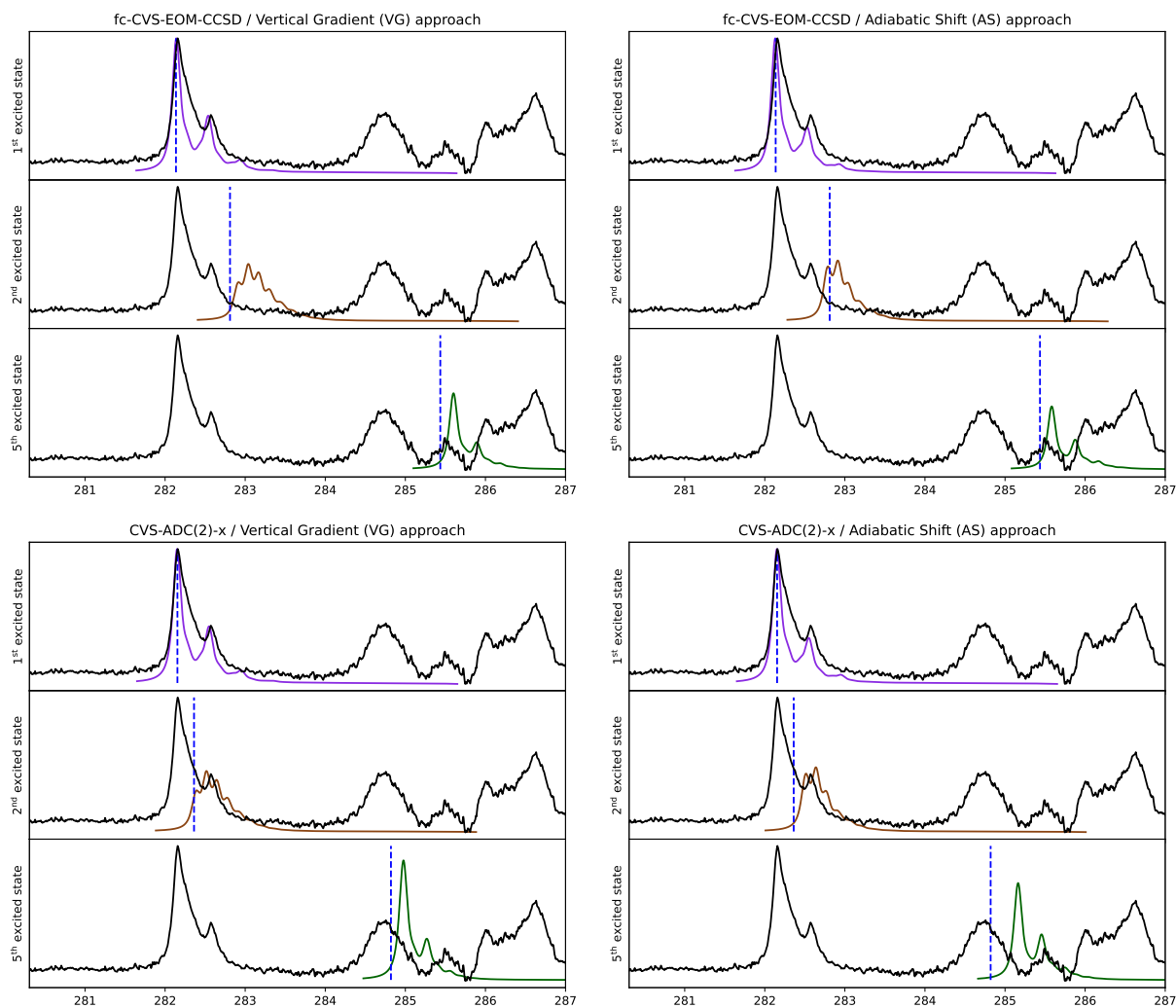


FIG. S4. Vibrationally resolved spectral bands from a time-dependent approach based on (left) the Vertical Gradient approximation for the potential energy surfaces (PES), and (right) the Adiabatic Shift approximation. Top: Excitation energies and electronic transition densities from fc-CVS-EOM-CCSD. Bottom: excitation energies and electronic transition densities from CVS-ADC(2)-x. The spectral bands were broadened by a Voigt function with a Gaussian broadening of 100 meV and Lorentzian broadening of 50 meV. The fc-CVS-EOM-CCSD VG spectra are shifted by +200 meV and the fc-CVS-EOM-CCSD AS spectra by +250 meV. The CVS-ADC(2)-x VG results are shifted by +175 meV and the CVS-ADC(2)-x AS results were shifted by +318 meV. Vertical lines correspond to the excitations energies of Figs. S2 and S3, and of Fig. 4 of the main paper.

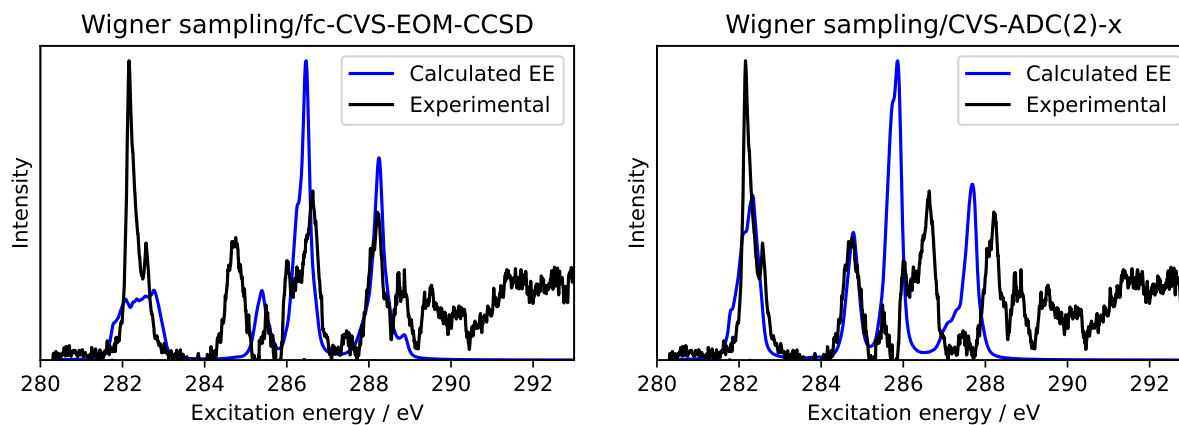


FIG. S5. Comparison between experimental NEXAFS spectrum (black line) and the Wigner sampling at 300 K consisting of 200 geometries in blue. Calculations were performed at the (left) fc-CVS-EOM-CCSD/aug-cc-pVTZ and (right) CVS-ADC(2)-x/aug-cc-pVTZ level of theory.

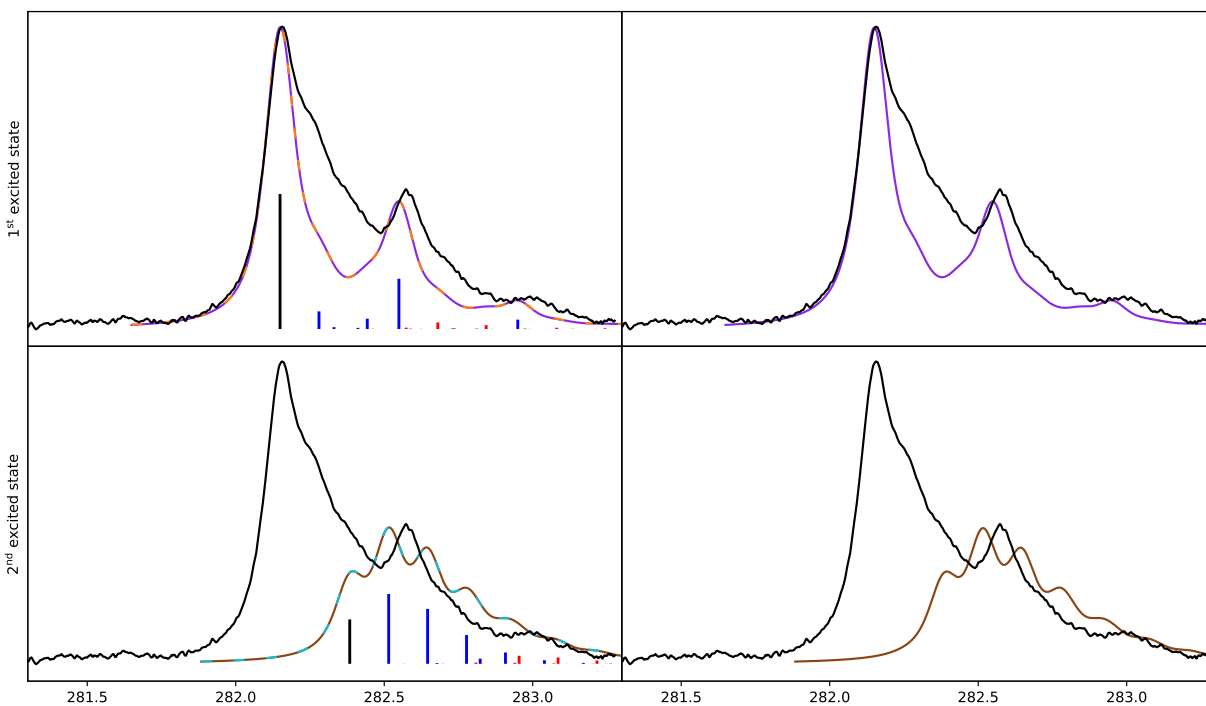


FIG. S6. Comparison between the high-resolution experimental NEXAFS spectrum (black line) and vibrational structure of the first and second CVS-ADC(2)-x electronic transitions at temperatures of 0 K (left) and 300 K (right). For 0 K the results were obtained by the TI (dashed orange and turquoise line) and TD approach (violet and brown line) while only the TD approach was employed at 300 K. The PES were obtained from the Vertical Gradient approximation. The colors of the sticks correspond to the number of different vibrational modes involved in a transition; blue sticks consists of one vibrational mode, red sticks consists of two vibrational modes, and green sticks consists of three vibrational modes. The spectra have been shifted by +175 meV to align with the first experimental peak. The spectral bands were broadened by a Voigt function with a Gaussian FWHM of 50 meV and a Lorentzian FWHM of 100 meV.

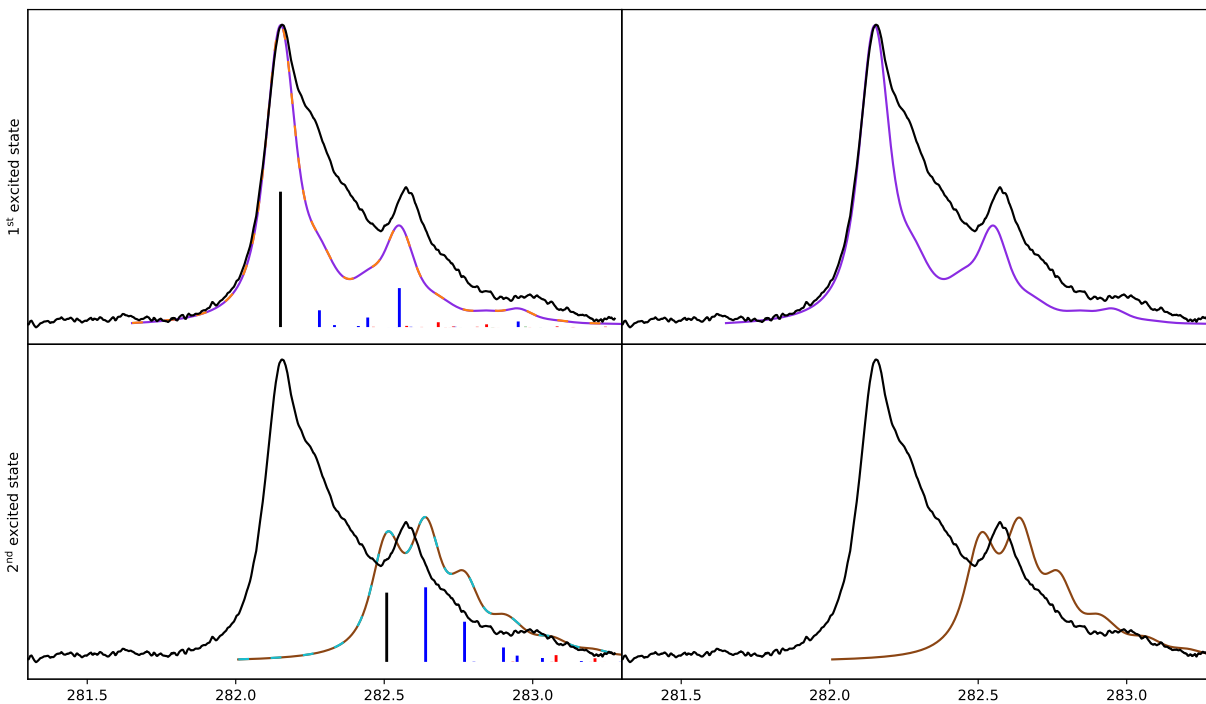


FIG. S7. Comparison between the high-resolution experimental NEXAFS spectrum (black line) and vibrational structure of the first and second CVS-ADC(2)-x electronic transitions at temperatures of 0 K (left) and 300 K (right). For 0 K the results were obtained by the TI (dashed orange and turquoise line) and TD approach (violet and brown line) while only the TD approach was employed at 300 K. The PES were obtained from the Adiabatic Shift approximation. The colors of the sticks correspond to the number of different vibrational modes involved in a transition; blue sticks consists of one vibrational mode, red sticks consists of two vibrational modes, and green sticks consists of three vibrational modes. The spectra have been shifted by +318 meV to align with the first experimental peak. The spectral bands were broadened by a Voigt function with a Gaussian FWHM of 50 meV and a Lorentzian FWHM of 100 meV.

TABLE S7. Vibrational modes of the propargyl radical and their frequencies in cm^{-1} as obtained on the MP2/aug-cc-pVDZ level of theory. An illustration of these modes can be found in Fig. S8.

Vibration	Symmetry	Description	Energy (cm^{-1})
mode 12	A ₁	C3-H stretching	3542.59
mode 11	B ₁	asymm. -CH ₂ stretching	3349.32
mode 10	A ₁	symm. -CH ₂ stretching	3227.90
mode 9	A ₁	C3-C2 stretching	2369.24
mode 8	A ₁	-CH ₂ scissoring	1465.92
mode 7	A ₁	C1-C2 stretching	1057.24
mode 6	B ₁	in-plane rocking @C1	1048.32
mode 5	B ₁	in-plane rocking @C3	768.244
mode 4	B ₂	oop (\perp) wagging @C3	681.703
mode 3	B ₂	oop (\perp) wagging -CH ₂	623.043
mode 2	B ₂	oop bending @C2 (wagging)	399.720
mode 1	B ₁	in-plane rocking @C2	258.101

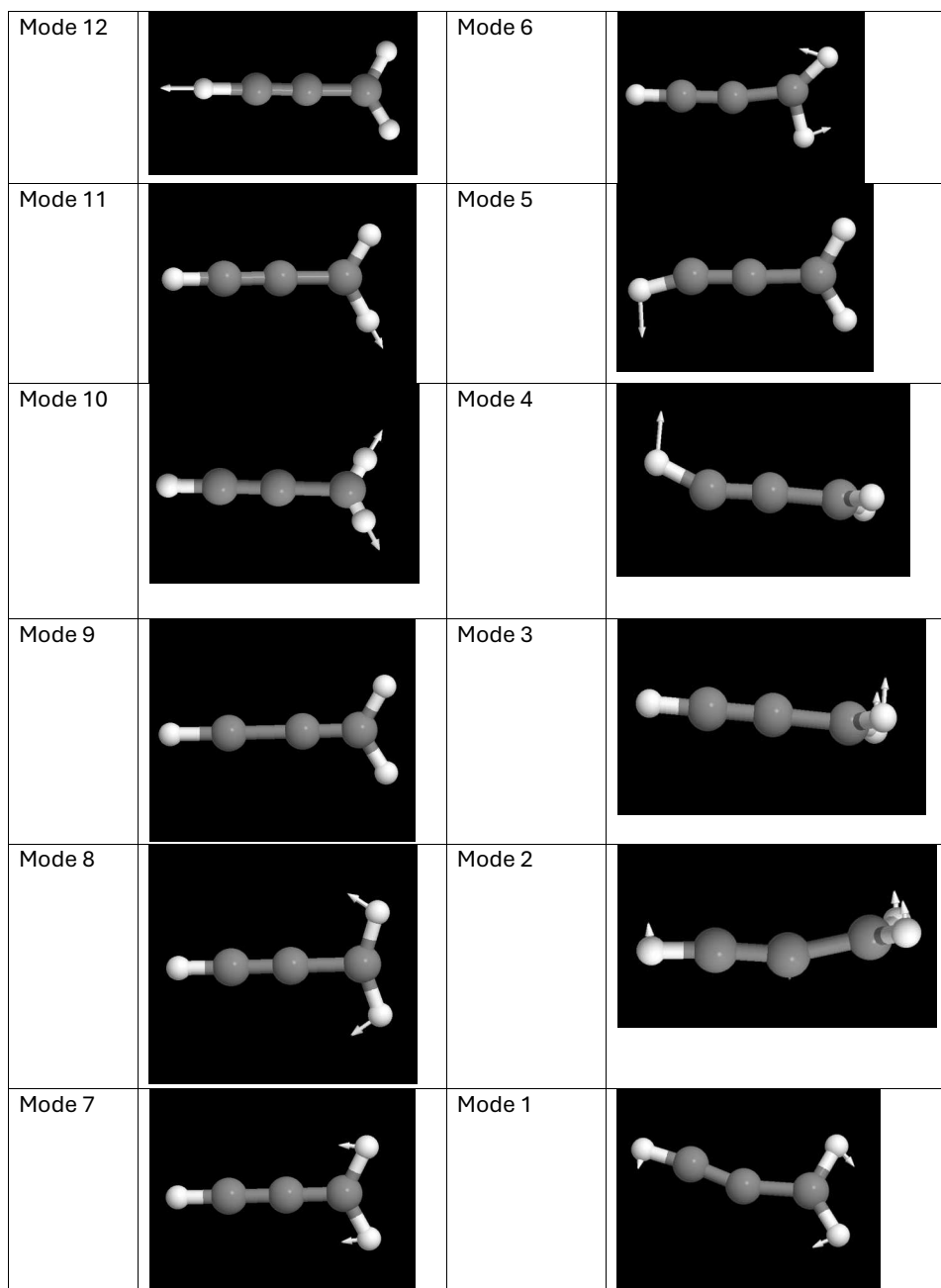


FIG. S8. Illustration of the fundamental modes of the propargyl radical as specified in Table S7.

S2.7. Optimized structures

TABLE S8. Bond lengths (in Å) for the ground state [optimized both at CCSD(T*)-F12a/cc-pVQC-F12 (from Ref. 4) and fc-MP2/aug-cc-pVDZ (this work) levels] and the first three bright core excited states (optimized using CVS-ADC(2)-x/aug-cc-pVDZ, this work) of the propargyl radical. The semi-experimental bond-lengths for the ground state from Ref. 22 are also reported for comparison.

State/method/basis	C1–H1/2	C1–C2	C2–C3	C3–H3
GS/CCSD(T*)-F12a/cc-pVQC-F12 ⁴	1.07997	1.37722	1.22507	1.06302
GS/semi-experimental ²²	1.0789(1)	1.3749(4)	1.2220(4)	1.0610(2)
GS/fc-MP2/aug-cc-pVDZ	1.08723	1.40144	1.20988	1.07130
1 st /CVS-ADC(2)-x/aug-cc-pVDZ	1.03232	1.38785	1.19007	1.06943
2 nd /CVS-ADC(2)-x/aug-cc-pVDZ	1.08436	1.31830	1.21496	1.02749
5 th /CVS-ADC(2)-x/aug-cc-pVDZ	1.09665	1.35510	1.25539	1.05839

Ground state (\tilde{X}^2B_1)/fc-MP2/aug-cc-pVDZ

Ground state energy: -115.7801414328 Ha.
1st excited state energy: -105.4107274234 Ha. (E_exc: 282.166 eV)
2nd excited state energy: -105.3995097829 Ha. (E_exc: 282.472 eV)
5th excited state energy: -105.3096408480 Ha. (E_exc: 284.917 eV)

C1	0.000000000000	0.000000000000	1.268908999959
C2	0.000000000000	0.000000000000	-0.134232999996
C3	0.000000000000	0.000000000000	-1.344778999957
H1	-0.940295999970	0.000000000000	1.816694999942
H2	0.940295999970	0.000000000000	1.816694999942
H3	0.000000000000	0.000000000000	-2.416981999922

First excited state (1^2A_1)/CVS-ADC(2)-x/aug-cc-pVDZ

Energy: -105.4229786608 Ha. (E_adia: 281.833 eV)

C1	-0.000109386715	0.000000000000	1.260963322953
C2	-0.000131754750	-0.000000000000	-0.126882435583
C3	0.000040587964	-0.000000000000	-1.316950220391
H1	-0.887534699379	0.000000000000	1.788009294302
H2	0.887588569164	-0.000000000000	1.787545919345
H3	0.000146683717	-0.000000000000	-2.386380880667

Second excited state (2^2A_1)/CVS-ADC(2)-x/aug-cc-pVDZ

Energy: -105.4098358009 Ha. (E_adia: 282.190 eV)

C1	-0.000018395481	0.000000000000	1.226614758055
C2	-0.000012583657	-0.000000000000	-0.091682480706
C3	-0.000075431347	-0.000000000000	-1.306642411737
H1	-0.946311572364	0.000000000000	1.756118582801
H2	0.946332709390	0.000000000000	1.756027123128
H3	0.000085273461	-0.000000000000	-2.334130571527

Fifth excited state (third bright) (2^2A_2)/CVS-ADC(2)-x/aug-cc-pVDZ

Energy: -105.3123007185 (E_adia: 284.845 eV)

C1	-0.000000000000	0.000000000000	1.251064629150
C2	0.000000000002	0.000000000000	-0.104036636939
C3	-0.000000000003	-0.000000000000	-1.359426986977
H1	-0.938578669184	0.000000000000	1.818259546634
H2	0.938578669181	-0.000000000000	1.818259546637
H3	0.000000000002	-0.000000000000	-2.417815098541

Ground state (\tilde{X}^2B_1) gradient

0.00000000E+00	0.00000000E+00	-1.76300000E-04
0.00000000E+00	0.00000000E+00	-2.76190000E-04
0.00000000E+00	0.00000000E+00	1.20780000E-04
6.29100000E-05	0.00000000E+00	1.31660000E-04
-6.29100000E-05	0.00000000E+00	1.31660000E-04
0.00000000E+00	0.00000000E+00	6.83900000E-05

First excited state/VG gradient (1^2A_1)

0.	0.	-0.0279717
-0.	0.	0.0434325
0.	-0.	-0.0582662
-0.0405327	-0.	0.0224284
0.0405327	0.	0.0224284
-0.	0.	-0.0020514

First excited state/AS gradient (1^2A_1)

-0.0000275	0.	0.0000821
0.0000149	-0.	0.0001105
0.0000035	0.	-0.0001316
0.0000617	-0.	-0.0000189
-0.0000526	0.	-0.0000464
-0.0000002	0.	0.0000043

Second excited state/VG gradient (2^2A_1)

-0.	0.	0.064691
0.	-0.	-0.0734743
-0.	0.	0.0357863
-0.0000707	0.	0.0060424
0.0000707	-0.	0.0060424
0.	-0.	-0.0390877

Second excited state/AS gradient (2^2A_1)

-0.0000093	-0.	0.0000169
0.0000104	0.	-0.000017
-0.0000088	-0.	0.0000254
-0.0000003	-0.	-0.0000041
0.0000042	0.	-0.0000073
0.0000038	-0.	-0.0000139

Fifth excited state/VG gradient (2^2A_2)

0.	0.	0.0291388
-0.	-0.	-0.1115036
0.	0.	0.0938297
-0.0032512	-0.	-0.0014204
0.0032512	0.	-0.0014204
-0.	-0.	-0.008624

Fifth excited state/AS gradient (2^2A_2)

0.	-0.	0.0000031
-0.	0.	0.0000032
0.	-0.	0.0000081
-0.0000002	0.	0.0000003
0.0000002	-0.	0.0000003
-0.	-0.	-0.000015

Ground state (\tilde{X}^2B_1) Hessian (used as excited state Hessian for VG and AS)

6.52783110E-01	0.00000000E+00	5.14137200E-02	0.00000000E+00	0.00000000E+00
6.14648070E-01	-8.54368300E-02	0.00000000E+00	0.00000000E+00	1.06219140E-01
0.00000000E+00	-3.26353300E-02	0.00000000E+00	0.00000000E+00	5.78502400E-02
-2.50000000E-07	0.00000000E+00	-2.43717860E-01	1.40000000E-07	0.00000000E+00
1.52805322E+00	6.89528000E-03	0.00000000E+00	0.00000000E+00	-3.52666100E-02
0.00000000E+00	-3.00000000E-08	5.70601600E-02	0.00000000E+00	4.61399000E-03
0.00000000E+00	0.00000000E+00	-3.18150700E-02	0.00000000E+00	0.00000000E+00
4.73997900E-02	2.50000000E-07	0.00000000E+00	-1.14237770E-01	-1.50000000E-07
0.00000000E+00	-1.27217487E+00	3.00000000E-08	0.00000000E+00	1.83390845E+00
-2.91589690E-01	0.00000000E+00	1.34164210E-01	7.00990000E-03	0.00000000E+00
-1.54037000E-03	-5.12740000E-04	0.00000000E+00	-2.47472000E-03	2.97539300E-01
0.00000000E+00	-1.41775700E-02	0.00000000E+00	0.00000000E+00	2.62153000E-03
0.00000000E+00	0.00000000E+00	5.74010000E-04	0.00000000E+00	0.00000000E+00
5.38284000E-03	1.33176130E-01	0.00000000E+00	-1.29106600E-01	2.69865100E-02
0.00000000E+00	-7.41189000E-03	-8.96110000E-04	0.00000000E+00	-9.01005000E-03
-1.44068000E-01	0.00000000E+00	1.35099830E-01	-2.91589690E-01	0.00000000E+00
-1.34164200E-01	7.00990000E-03	0.00000000E+00	1.54037000E-03	-5.12740000E-04
0.00000000E+00	2.47472000E-03	-1.22295000E-02	0.00000000E+00	-1.38866100E-02
2.97539300E-01	0.00000000E+00	-1.41778100E-02	0.00000000E+00	0.00000000E+00
2.62182000E-03	0.00000000E+00	0.00000000E+00	5.74090000E-04	0.00000000E+00
0.00000000E+00	5.41794000E-03	0.00000000E+00	0.00000000E+00	5.38281000E-03
-1.33176150E-01	0.00000000E+00	-1.29106600E-01	-2.69864900E-02	0.00000000E+00
-7.41189000E-03	8.96100000E-04	0.00000000E+00	-9.01005000E-03	1.38866100E-02
0.00000000E+00	1.04793800E-02	1.44068000E-01	0.00000000E+00	1.35099830E-01
8.93781000E-03	0.00000000E+00	0.00000000E+00	4.64510000E-04	0.00000000E+00
1.40000000E-07	-2.76633500E-02	0.00000000E+00	-1.40000000E-07	-2.17270000E-04
0.00000000E+00	-1.31192000E-03	-2.17270000E-04	0.00000000E+00	1.31193000E-03
1.86955700E-02	0.00000000E+00	4.96299000E-03	0.00000000E+00	0.00000000E+00
1.35682000E-03	0.00000000E+00	0.00000000E+00	-2.13468100E-02	0.00000000E+00
0.00000000E+00	1.81250000E-04	0.00000000E+00	0.00000000E+00	1.81160000E-04

0.00000000E+00	0.00000000E+00	1.46645800E-02	2.00000000E-08	0.00000000E+00
1.52076000E-03	-1.00000000E-08	0.00000000E+00	2.66329000E-03	0.00000000E+00
0.00000000E+00	-4.29475710E-01	3.22700000E-05	0.00000000E+00	-5.06700000E-05
-3.22700000E-05	0.00000000E+00	-5.06700000E-05	0.00000000E+00	0.00000000E+00
4.25393020E-01				

S2.8. FCclasses3 input file example

As an example of the construction of the input files for `fcclasses3`, we here provide the general structure of the input for the Adiabatic Shift of the first excited state

1. *fcc.inp*

```
$$$  
PROPERTY      =   OPA  
MODEL         =   AS  
DIPOLE        =   FC  
TEMP          =   0.00  
BROADFUN      =   VOI  
HWHM          =   0.025  
HWHM2         =   0.05  
METHOD        =   TD  
NORMALMODES   =   COMPUTE  
COORDS        =   CARTESIAN  
STATE1_FILE   =   GS.fcc  
STATE2_FILE   =   ES.fcc  
ELDIP_FILE    =   eldip
```

2. *ES.fcc*

```
GEOM          UNITS=ANGS  
6
```

```
First excited state/CVS-ADC(2)-x/aug-cc-pVDZ
```

```
ENER          UNITS=AU  
-105.4229786608
```

```
GRAD          UNITS=AU
```

First excited state/AS gradient

3. *GS,fcc*

GEOM UNITS=ANGS

6

Ground state/fc-MP2/aug-cc-pVDZ

ENER UNITS=AU

-115.7801414328

GRAD UNITS=AU

Ground state gradient

HESS UNITS=AU

Ground state Hessian

4. *eldip*

0.000000 1.000000 0.000000

0.000000 1.000000 0.000000

REFERENCES

- ¹D. Schaffner, T. Juncker von Buchwald, E. Karaev, M. Alagia, R. Richter, S. Stranges, S. Coriani, and I. Fischer, *J. Chem. Phys.* **161**, 034309 (2024).
- ²M. L. Vidal, X. Feng, E. Epifanovsky, A. I. Krylov, and S. Coriani, *J. Chem. Theory Comput.* **15**, 3117 (2019).
- ³E. Epifanovsky, A. T. B. Gilbert, X. Feng, J. Lee, Y. Mao, N. Mardirossian, P. Pokhilko, A. F. White, M. P. Coons, A. L. Dempwolff, Z. Gan, D. Hait, P. R. Horn, L. D. Jacobson, I. Kaliman, J. Kussmann, A. W. Lange, K. U. Lao, D. S. Levine, J. Liu, S. C. McKenzie, A. F. Morrison, K. D. Nanda, F. Plasser, D. R. Rehn, M. L. Vidal, Z.-Q. You, Y. Zhu, B. Alam,

B. J. Albrecht, A. Aldossary, E. Alguire, J. H. Andersen, V. Athavale, D. Barton, K. Begam, A. Behn, N. Bellonzi, Y. A. Bernard, E. J. Berquist, H. G. A. Burton, A. Carreras, K. Carter-Fenk, R. Chakraborty, A. D. Chien, K. D. Closser, V. Cofer-Shabica, S. Dasgupta, M. de Wergifosse, J. Deng, M. Diedenhofen, H. Do, S. Ehlert, P.-T. Fang, S. Fatehi, Q. Feng, T. Friedhoff, J. Gayvert, Q. Ge, G. Gidofalvi, M. Goldey, J. Gomes, C. E. González-Espinoza, S. Gulania, A. O. Gunina, M. W. D. Hanson-Heine, P. H. P. Harbach, A. Hauser, M. F. Herbst, M. Hernández Vera, M. Hodecker, Z. C. Holden, S. Houck, X. Huang, K. Hui, B. C. Huynh, M. Ivanov, A. Jász, H. Ji, H. Jiang, B. Kaduk, S. Kähler, K. Khistyayev, J. Kim, G. Kis, P. Klunzinger, Z. Koczor-Benda, J. H. Koh, D. Kosenkov, L. Koulias, T. Kowalczyk, C. M. Krauter, K. Kue, A. Kunitsa, T. Kus, I. Ladjánszki, A. Landau, K. V. Lawler, D. Lefrancois, S. Lehtola, R. R. Li, Y.-P. Li, J. Liang, M. Liebenthal, H.-H. Lin, Y.-S. Lin, F. Liu, K.-Y. Liu, M. Loipersberger, A. Luenser, A. Manjanath, P. Manohar, E. Mansoor, S. F. Manzer, S.-P. Mao, A. V. Marenich, T. Markovich, S. Mason, S. A. Maurer, P. F. McLaughlin, M. F. S. J. Menger, J.-M. Mewes, S. A. Mewes, P. Morgante, J. W. Mullinax, K. J. Oosterbaan, G. Paran, A. C. Paul, S. K. Paul, F. Pavošević, Z. Pei, S. Prager, E. I. Proynov, Á. Rák, E. Ramos-Cordoba, B. Rana, A. E. Rask, A. Rettig, R. M. Richard, F. Rob, E. Rossomme, T. Scheele, M. Scheurer, M. Schneider, N. Sergueev, S. M. Sharada, W. Skomorowski, D. W. Small, C. J. Stein, Y.-C. Su, E. J. Sundstrom, Z. Tao, J. Thirman, G. J. Tornai, T. Tsuchimochi, N. M. Tubman, S. P. Veccham, O. Vydrov, J. Wenzel, J. Witte, A. Yamada, K. Yao, S. Yeganeh, S. R. Yost, A. Zech, I. Y. Zhang, X. Zhang, Y. Zhang, D. Zuev, A. Aspuru-Guzik, A. T. Bell, N. A. Besley, K. B. Bravaya, B. R. Brooks, D. Casanova, J.-D. Chai, S. Coriani, C. J. Cramer, G. Cserey, A. E. DePrince, R. A. DiStasio, A. Dreuw, B. D. Dunietz, T. R. Furlani, W. A. Goddard, S. Hammes-Schiffer, T. Head-Gordon, W. J. Hehre, C.-P. Hsu, T.-C. Jagau, Y. Jung, A. Klamt, J. Kong, D. S. Lambrecht, W. Liang, N. J. Mayhall, C. W. McCurdy, J. B. Neaton, C. Ochsenfeld, J. A. Parkhill, R. Peverati, V. A. Rassolov, Y. Shao, L. V. Slipchenko, T. Stauch, R. P. Steele, J. E. Subotnik, A. J. W. Thom, A. Tkatchenko, D. G. Truhlar, T. Van Voorhis, T. A. Wesolowski, K. B. Whaley, H. L. Woodcock, P. M. Zimmerman, S. Faraji, P. M. W. Gill, M. Head-Gordon, J. M. Herbert, and A. I. Krylov, *J. Chem. Phys.* **155**, 084801 (2021).

⁴P. Botschwina and R. Oswald, *Chem. Phys.* **378**, 4 (2010).

⁵T. B. Adler, G. Knizia, and H.-J. Werner, *J. Chem. Phys.* **127**, 221106 (2007).

⁶G. Knizia, T. B. Adler, and H.-J. Werner, *J. Chem. Phys.* **130**, 054104 (2009).

⁷K. A. Peterson, T. B. Adler, and H.-J. Werner, *J. Chem. Phys.* **128**, 084102 (2008).

- ⁸T. Clark, J. Chandrasekhar, G. W. Spitznagel, and P. V. R. Schleyer, *J. Comput. Chem.* **4**, 294 (1983).
- ⁹R. Krishnan, J. S. Binkley, R. Seeger, and J. A. Pople, *J. Chem. Phys.* **72**, 650 (1980).
- ¹⁰O. Marchetti and H.-J. Werner, *Phys. Chem. Chem. Phys.* **10**, 3400 (2008).
- ¹¹T. H. Dunning, *J. Chem. Phys.* **90**, 1007 (1989).
- ¹²R. A. Kendall, T. H. Dunning, and R. J. Harrison, *J. Chem. Phys.* **96**, 6796 (1992).
- ¹³A. I. Krylov, *J. Chem. Phys.* **153**, 080901 (2020).
- ¹⁴J. Cerezo and F. Santoro, *J. Comput. Chem.* **44**, 626 (2023).
- ¹⁵P. Macak, Y. Luo, and H. Ågren, *Chem. Phys. Lett.* **330**, 447 (2000).
- ¹⁶M. Biczysko, J. Bloino, F. Santoro, and V. Barone, in *Computational strategies for spectroscopy* (Wiley Online Library, 2012) pp. 361–443.
- ¹⁷I. E. Brumboiu, “cvs-adc-grad,” <https://gitlab.com/iubr/cvs-adc-grad> (2025).
- ¹⁸M. F. Herbst, M. Scheurer, T. Fransson, D. R. Rehn, and A. Dreuw, *WIREs Comput. Mol. Sci.* **10**, e1462 (2020).
- ¹⁹Q. Sun, T. C. Berkelbach, N. S. Blunt, G. H. Booth, S. Guo, Z. Li, J. Liu, J. D. McClain, E. R. Sayfutyarova, S. Sharma, S. Wouters, and G. K.-L. Chan, *WIREs Comput. Mol. Sci.* **8**, e1340 (2018).
- ²⁰Q. Sun, X. Zhang, S. Banerjee, P. Bao, M. Barbry, N. S. Blunt, N. A. Bogdanov, G. H. Booth, J. Chen, Z.-H. Cui, J. J. Eriksen, Y. Gao, S. Guo, J. Hermann, M. R. Hermes, K. Koh, P. Koval, S. Lehtola, Z. Li, J. Liu, N. Mardirossian, J. D. McClain, M. Motta, B. Mussard, H. Q. Pham, A. Pulkin, W. Purwanto, P. J. Robinson, E. Ronca, E. R. Sayfutyarova, M. Scheurer, H. F. Schurkus, J. E. T. Smith, C. Sun, S.-N. Sun, S. Upadhyay, L. K. Wagner, X. Wang, A. White, J. D. Whitfield, M. J. Williamson, S. Wouters, J. Yang, J. M. Yu, T. Zhu, T. C. Berkelbach, S. Sharma, A. Y. Sokolov, and G. K.-L. Chan, *J. Chem. Phys.* **153**, 024109 (2020).
- ²¹DTU Computing Center, “DTU Computing Center resources,” (2024), <https://doi.org/10.48714/DTU.HPC.0001>.
- ²²P. B. Changala, P. R. Franke, J. F. Stanton, G. B. Ellison, and M. C. McCarthy, *J. Am. Chem. Soc.* **146**, 1512 (2024).